

SGP-TR-184

# **Experimental Measurement of Two-Phase Relative Permeabilities in Synthetic Vertical Fractures**

**Nicholas Speyer**

June 2007

Financial support was provided through the  
Stanford Geothermal Program under  
Department of Energy Grant No. DE-FG36-02ID14418,  
and by the Department of Petroleum Engineering,  
Stanford University



Stanford Geothermal Program  
Interdisciplinary Research in  
Engineering and Earth Sciences  
STANFORD UNIVERSITY  
Stanford, California



## **Abstract**

Relative permeability characteristics in porous media have been studied extensively and are reasonably well understood. However there have been comparatively few studies of relative permeability in fractures. Given that geothermal reservoir permeabilities are almost always dominated by fractures, understanding of fracture relative permeabilities is essential for accurate geothermal reservoir simulation. Two-phase fracture flow was simulated using an artificial fracture created between an aluminum plate and a sheet of glass. The experiments simulated horizontal flow in a vertical fracture to compare with the work of Chen (2005) who made similar measurements on the same apparatus oriented horizontally. N<sub>2</sub>-water, steam-water, and CO<sub>2</sub>-water relative permeabilities were measured using both smooth and rough glass. Measured relative permeabilities were compared with the work of Chen and with known relative permeability models.



## Acknowledgments

There are several people who need to be acknowledged for their contributions to this work and for helping to make these years at Stanford as positive as they have been.

My predecessor Allan Chen was very helpful, especially in helping me get on my feet and familiarize myself with the experimental apparatus and Matlab codes. Laura Garner has been instrumental in providing administrative support and helping me order all of the equipment I needed. Aldo helped to design and then constructed the frame for mounting the fracture apparatus vertically. Kewen Li and the rest of the geothermal group both past and present have my gratitude for all of the helpful advice they have provided in Thursday meetings and in the laboratory.

I am most grateful to my advisor, Roland Horne. Roland has guided me through my research here at Stanford with kindness and insight. Most important though has been his patience, especially at the beginning of my research. Getting the apparatus working and performing these experiments was slow-going at best and Roland helped me through every stage.

Thank you to my classmates in the M.S. class of 2007. They have inspired me to work harder and to slack off at all of the right and wrong times over the last two years. They are always ready to offer creative insights into schoolwork and research or to run across campus for a free lunch from SUPRI meeting leftovers. Coming to Stanford, I expected to get an excellent education, but I did not expect to make such great friends.

I also must thank my parents. They taught me to work hard and to do my very best, a lesson that took a while to drive home. They have stood behind me through every stage of my education and my life and I am forever grateful.

Finally, I must thank Carly. Your love has supported me through every single day of this challenge. No matter what homeworks, projects, deadlines, or laboratory malfunctions have my head spinning, coming home to you makes every day wonderful. This work is dedicated to you.



# Contents

1. Introduction.....	1
1.1. Background.....	2
1.1.1. Previous Work .....	2
1.1.2. Relative Permeability Concepts and Models .....	3
1.2. Why is Relative Permeability Important?.....	7
2. N <sub>2</sub> -Water and CO <sub>2</sub> -Water Relative Permeability Measurements .....	9
2.1. Experimental Apparatus .....	9
2.1.1. Fracture Apparatus.....	9
2.1.2. Fluid Injection System .....	12
2.1.3. Pressure and Temperature Measurements .....	14
2.1.4. Saturation Measurements.....	15
2.2. Experimental Procedure.....	18
2.2.1. Fracture Dilation Test .....	18
2.2.2. Relative Permeability Measurements .....	19
2.3. Results.....	19
2.3.1. Relative Permeability Data .....	19
2.3.2. Smooth-Walled Observations .....	23
2.3.3. Rough-Walled Observations.....	24
2.4. Discussion .....	26
2.5. Comparison with Established Relative Permeability Models.....	27
2.5.1. Smooth-Walled Fracture.....	27
2.5.2. Rough-Walled Fracture.....	29
3. Steam-Water Relative Permeability Measurements .....	30
3.1. Experimental Apparatus .....	30
3.1.1. FFRD Apparatus .....	31
3.1.2. Pressure Measurements.....	34
3.1.3. Back-Pressure Apparatus .....	35
3.2. Procedure .....	36
3.3. Results.....	37
3.3.1. Smooth-Walled Relative Permeability Results.....	37
3.3.2. Rough-Walled Relative Permeability Results .....	39
3.3.3. Flow Observations .....	41
3.4. Discussion .....	45
3.4.1. Smooth-Walled Fracture.....	45
3.4.2. Rough-Walled Fracture.....	45
4. Conclusions and Future Work .....	47
A. Matlab Code for Image Capture .....	53
B. Matlab Code for S <sub>w</sub> Calculation (Rough-Walled).....	55

C. Matlab Codes for $S_w$ Calculation (Smooth-Walled) .....	58
D. FFRD Matlab Code.....	62

## List of Tables

Table 1. Range of reported static contact angles of water on glass and aluminum. (Chen, 2005) 12



## List of Figures

Figure 1-1. X-curve relative permeability model.	5
Figure 1-2. Corey and Brooks-Corey relative permeability models.	7
Figure 1-3. Viscous-coupling relative permeability model.	7
Figure 1-4. Using an inappropriate relative permeability model can result in expensive overestimations/underestimations of reservoir production capacity over time.	8
Figure 2-1. Diagram of fracture apparatus. (Modified from Diomampo, 2001 and Chen, 2005)	10
Figure 2-2. Description of the Homogeneously Rough (HR) glass surface. a) Two-dimensional surface pattern. b) Three-dimensional aperture profile (vertically exaggerated). c) Histogram of aperture distribution. d) Aperture along line A-A'. (Chen 2005)	11
Figure 2-3. Fluid supply and measurement apparatus.	13
Figure 2-4. Viscosity behavior of water, CO <sub>2</sub> , and N <sub>2</sub> at temperatures observed during gas-water relative permeability measurements.	14
Figure 2-5. Schematic of experimental apparatus and data acquisition system. (Chen, 2005)	16
Figure 2-6. Basic workflow for relative permeability measurements.	16
Figure 2-7. Example of saturation value estimation by processing images captured from digital video.	17
Figure 2-8. Example of kA behavior with changing fracture pressure.	19
Figure 2-9. Full and averaged data for CO <sub>2</sub> -water relative permeability in the smooth-walled fracture.	20
Figure 2-10. Full relative permeability data from smooth-walled N <sub>2</sub> -water experiments. Average values for each steady state are shown as well.	21

Figure 2-11. Full and average N <sub>2</sub> -water relative permeability data from Chen (2005) made with the same smooth-walled apparatus oriented horizontally.	21
Figure 2-12. Raw data from N <sub>2</sub> -water relative permeability measurements on the rough-walled fracture. Data are from a single run.	22
Figure 2-13. Averaged N <sub>2</sub> -water relative permeability data from the rough-walled fracture. Averaged data are from multiple runs.	22
Figure 2-14. Full and average N <sub>2</sub> -water relative permeability data from Chen (2005) made with the same rough-walled apparatus oriented horizontally.	23
Figure 2-15. CO <sub>2</sub> -water flow structures in the smooth-walled fracture with gas-water flow ratios increasing A-D. Flow structures were identical for N <sub>2</sub> and CO <sub>2</sub> . The dark phase is gas and the light phase is water.	25
Figure 2-16. N <sub>2</sub> -water flow structures in the rough-walled fracture with gas-water flow ratios increasing A-D. The color difference is the result of a changed camera setting half-way through the run. The dark phase is gas and the light phase is water.	25
Figure 2-17. Normalized CO <sub>2</sub> -water average relative permeability measurements compared with the X-curve and Corey-type curves.	28
Figure 2-18. Normalized N <sub>2</sub> -water average relative permeability measurements compared with the X-curve and Corey-type curves.	28
Figure 2-19. Averaged N <sub>2</sub> -water relative permeability data from two different runs compared with various known relative permeability models.	29
Figure 3-1. a) Schematic of FFRD device. b) Example of water and gas FFRD signals corresponding to actual flow (Chen 2005).	32
Figure 3-2. Sample histogram from FFRD data.	33
Figure 3-3. Calibration of the FFRD with known fractional flows.	34
Figure 3-4. Diagram illustrating the system for keeping the fluid in the pressure tubing cool.	35
Figure 3-5. Schematic of the back-pressure apparatus used in the steam-water experiments.	36
Figure 3-6. Example of movement of a steam bubble through water in a tube via the phase change mechanism. Steam forms on the down-pressure end of the bubble	

and condenses at the high-pressure end of the bubble, thus moving the location of the bubble without moving the actual mass in the tube.	37
Figure 3-7. Full and averaged steam-water relative permeability values for the smooth-walled fracture.	38
Figure 3-8. Averaged smooth-walled steam-water relative permeability data normalized and compared with established relative permeability models.	38
Figure 3-9. Comparison of normalized steam-water and N <sub>2</sub> -water relative permeability measurements with the smooth-walled fracture.	39
Figure 3-10. Average steam-water relative permeability values measured on the rough-walled fracture.	39
Figure 3-11. Averaged rough-walled steam-water relative permeability data normalized and compared with established relative permeability models.	40
Figure 3-12. Comparison of normalized steam-water and N <sub>2</sub> -water relative permeability measurements with the rough-walled fracture.	40
Figure 3-13. Air-water and steam-water horizontal-fracture relative permeabilities measured on: a) The smooth walled fracture b) The homogeneously rough-walled fracture. Data from Chen, (2005).	41
Figure 3-14. Static locally nucleated steam bubbles at very low steam-water flow ratios in the smooth-walled fracture. Steam is the dark phase.	42
Figure 3-15. Locally nucleated steam pockets (dark phase) migrating upward and in the direction of flow in the smooth-walled fracture, leaving behind two-phase trails (light gray).	42
Figure 3-16. Example of development and movement of steam structures in the smooth-walled fracture with high steam-water ratios. Each frame is separated by 0.4 seconds.	43
Figure 3-17. Example of steam-water flow structures in the rough-walled fracture with low steam-water flow ratios.	44
Figure 3-18. Example of steam-water flow structures in the rough-walled fracture with high steam-water flow ratios.	44



# Chapter 1

## 1. Introduction

Geothermal energy has been harnessed to produce electricity since early in the 20<sup>th</sup> century. Global geothermal generation capacity has steadily grown ever since, with approximately 10 GW of installed capacity today. This number is certain to grow as new technologies for identification and development of geothermal resources become available.

There are several advantages to generating electricity from geothermal energy over other energy sources. Unlike hydrocarbon and nuclear generation technologies, the fuel cost is zero. Also, geothermal energy is reliable base-load power. While solar and wind power output varies over the course of the day, geothermal power plants are almost always running at full capacity. Most importantly, geothermal power plants emit very little greenhouse gas, if any at all. In the context of the current global climate and energy crisis, with the need for reliable and cheap renewable energy sources becoming increasingly apparent, geothermal is a very attractive option.

There is some debate as to whether geothermal energy can be considered a renewable energy source. Geothermal reservoirs can be depleted to the point at which they will no longer produce electricity economically. However, if geothermal reservoirs are managed to optimize the life of a reservoir instead of to maximize profit, it is possible to generate electricity indefinitely. Furthermore, depleted reservoirs will recharge on a much shorter time-scale than hydrocarbon reserves (decades and centuries vs. millions of years).

Geothermal energy does have its downsides. High upfront capital costs and slow payouts make geothermal unattractive to many investors. In the long run geothermal power is very competitive, but that is not the only parameter that investors will consider. Another downside is that geothermal energy is geographically limited. Virtually all major geothermal developments in the world today are concentrated at the boundaries between tectonic plates and hot spots in the interiors of the plates (e.g. Hawaii). This is because those are the only locations where there is geothermal heat that has risen through enough of the crust to be economically recoverable with current drilling technologies. If one were to consider all of the heat inside the earth as recoverable, the worldwide geothermal resource would be astronomically large.

Unlike petroleum reservoirs, which are always found in sedimentary rocks, geothermal reservoirs are almost always found in igneous and metamorphic rock formations. This is not a coincidence. The same geologic activity that heats up the crust enough for us to recover thermal energy also causes volcanism and rock metamorphism. One of the most

critical reservoir parameters for any type of subsurface reservoir is permeability. In petroleum reservoirs, usually made of some kind of sedimentary rock, the permeability is dominated by the porous matrix. Due to the tightly packed crystalline nature of the rocks in geothermal reservoirs, there is virtually no matrix permeability, and any fluid that moves through such reservoirs moves through fractures. This is not to say that petroleum reservoirs are not fractured. All rocks formations anywhere near the surface of the earth are extensively fractured, including many petroleum reservoirs. But in geothermal reservoirs the permeability is almost always dominated by fracture networks.

Despite the prevalence of fractured rocks near the earth's surface, there is relatively little known about fluid flow in fractured media compared with the volumes of knowledge of flow in porous media, particularly relative permeability behavior. Relative permeability is the concept used to describe the way two or more phases flow together through the same space. Relative permeability of a particular phase is the permeability of a medium to that phase divided by the absolute permeability of the medium as shown in Equations 1 and 2:

$$k_{rw} = \frac{k_w}{k} \tag{1}$$

$$k_{rg} = \frac{k_g}{k} \tag{2}$$

Where  $k_{rw}$  and  $k_{rg}$  are the water and gas phase relative permeabilities, respectively,  $k$  is the absolute permeability of the medium, and  $k_w$  and  $k_g$  are the absolute permeabilities of the rock to water and gas, respectively. Relative permeability is not constant, but rather it varies with the saturation state of the medium (e.g.  $k_{rw}$  is higher with high water saturation than with low). Relative permeabilities are usually modeled as functions of wetting phase saturation,  $S_w$ .

## 1.1. Background

### 1.1.1. Previous Work

There have been several experimental studies that have investigated fracture relative permeabilities (Fourar et al., 1993; Persoff and Pruess, 1995; Diomampo, 2001; Chen 2005).

Fourar et al. (1993) measured relative permeability using a synthetic fracture consisting of two horizontal glass plates of varying textures. Different textures were created by gluing small glass beads to the surfaces. Water and gas were injected at set rates while pressure and saturation were measured. Flow was described according to three models: relative permeabilities, pipe flow, and as a homogeneous flow in a rough tube. High phase interference between gas and water was observed to the degree that the sum of the

two relative permeabilities was never equal to 1. It was also found that the relative permeabilities were not strict functions of  $S_w$ , but also depended on the liquid velocity in the fracture. Flow structures were observed and correlated with different flow rates and ratios.

Persoff and Pruess (1995) created a copy of a natural fracture by creating a mold of each side of a natural fracture and creating epoxy replicas from those molds. Relative permeability measurements were made and significant phase interference was again detected. Although the results did not match well with any of the major relative permeability models, it was concluded that treating fractures as very heterogeneous two-dimensional porous media was appropriate.

Diomampo (2001) measured nitrogen-water relative permeabilities in a horizontal fracture between glass and aluminum. High phase interference was observed as well as continuous instability of flow channels. A good match with the Corey-type relative permeability curves was found.

Chen (2005) conducted nitrogen-water and steam-water relative permeability experiments on the same apparatus and correlated different flow regimes to flow structures quantitatively. Steam relative permeabilities were seen to be greater than comparable nitrogen relative permeabilities due to phase transformation effects. The goal of the present work has been to build on the work of Chen and Diomampo in horizontal fractures, and determine the effect of fracture orientation by measuring relative permeabilities in horizontal flow through a vertical fracture.

### ***1.1.2. Relative Permeability Concepts and Models***

In this work, we make the assumption that generalized Darcy equations (Equations 3 and 4) can be used to describe flow rates in fractures. Inherent in this assumption is that fracture flow can be considered a case of flow through a two-dimensional porous medium. An alternative to this hypothesis would be to treat fracture flow as an extreme case of pipe flow (i.e. a very wide and flat pipe).

$$q_w = \frac{k_{abs} A k_{rw} (p_i - p_o)}{\mu_w L} \quad (3)$$

$$q_g = \frac{k_{abs} A k_{rg} (p_i - p_o)}{\mu_g L} \quad (4)$$

where  $l$  and  $g$  indicate liquid and gas respectively,  $k_{abs}$  is the absolute permeability of the fracture,  $p_i$  and  $p_o$  are the respective pressures at the inlet and outlet of the fracture,  $\mu$  is the viscosity, and  $L$  is the length of the fracture. In order to consider the compressibility of the gas phase, Equation (4) can be written as:

$$q_g = \frac{k_{abs} A k_{rg} (p_i^2 - p_o^2)}{2\mu_g p_o L} \quad (5)$$

The theoretical absolute permeability of a fracture with aperture  $h$  can be derived to be:

$$k_{abs} = \frac{h^2}{12} \quad (6)$$

Relative permeability describes the permeability of one phase in the presence of another. In the absence of any phase interference, the sum of  $k_{rg}$  and  $k_{rw}$  will be 1. This is rarely the case in real rocks. The interference effect can be quantified by the difference between 1 and the sum of the two relative permeabilities. In general, the lower is the sum of the two relative permeabilities, the greater is the phase interference.

Accurate reservoir simulation and forecasting cannot take place without some knowledge of the relative permeability characteristics. The relative permeabilities are commonly expressed as functions of the saturations, end-point values and irreducible saturations of the different fluids in three different models. The simplest model is the X-model, which assumes no interference between phases, and pure laminar flow (i.e. gas and water flowing parallel next to each other):

$$k_{rw} = S_w \quad (7)$$

$$k_{rg} = 1 - S_w \quad (8)$$

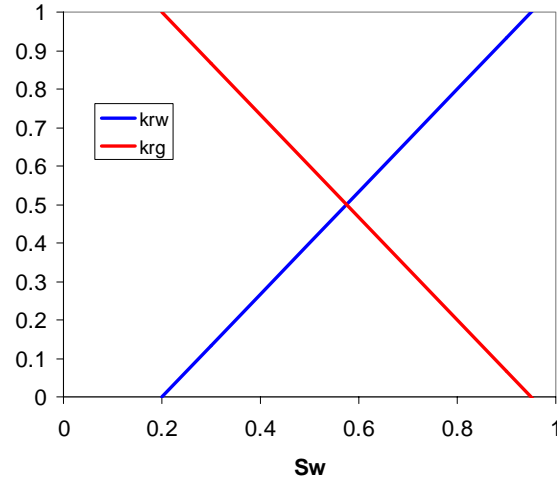


**Figure 1-1. X-curve relative permeability model.**

with  $S_w$  and  $S_g$  being the mobile water and gas saturations respectively. This model has the sum of  $k_{rg}$  and  $k_{rw}$  equal to 1. In real fractures, interactions between fluids and between fluids and the fracture surface can have an interference effect on the relative permeabilities, so a more comprehensive model may be more appropriate.

Traditionally, relative permeabilities in fractures used to be assumed to follow an X-curve with the relative permeability of each phase equal to the mobile saturation of that phase. The popularity of the X-curve may be largely due to its mathematical simplicity and to a lack of a definitive fracture relative permeability model. However, several studies have shown (Chen 2005, Diomampo 2001, Fourar et al. 1993, Persoff and Pruess 1995) that even in unrealistically smooth horizontal fractures, there is significant phase interference, which results in relative permeabilities that resemble Brooks-Corey (1966), or Corey (1954) relative permeabilities, which are described later (Figure 1-2).

In earlier experiments on horizontal fractures, relative permeabilities have been found to be very similar to the Corey curves used for relative permeability in homogeneously porous media (Diomampo, 2001; Chen, 2005):

$$k_{rl} = (S^*)^4 \quad (9)$$

$$k_{rg} = (1 - S^*)^2 (1 - S^{*2}) \quad (10)$$

with  $S^*$  defined as the mobile saturation:

$$S^* = \frac{(S_l - S_{rl})}{(1 - S_{rl} - S_{rg})} \quad (11)$$

with  $S_{rl}$  and  $S_{rg}$  being the irreducible residual saturations of liquid and gas respectively.

The Brooks-Corey model is also very popular for modeling relative permeability behavior in porous media:

$$k_{rw} = (S_w^*)^{(2+3\lambda)/\lambda} \quad (12)$$

$$k_{rg} = (1 - S_w^*)^2 [1 - (S_w^*)^{(2+\lambda)/\lambda}] \quad (13)$$

with  $\lambda$  being the pore size distribution index. This index should be small for very heterogeneous media and large for very homogenous media. Considering a smooth-walled fracture,  $\lambda$  can be considered to approach infinity. A typical  $\lambda$  value for a porous medium is 2, which when substituted into Equations 12 and 13 leaves us with the Corey model. This can be said to approximate the conditions of a rough-walled fracture. For a smooth-walled fracture with  $\lambda$  equal to infinity, we can derive the uniform pore-space (fracture) Brooks-Corey model:

$$k_{rw} = (S_w^*)^3 \quad (14)$$

$$k_{rg} = (1 - S_w^*)^3 \quad (15)$$

Another model treats the fracture like a system of pipes, incorporating the viscosities of the two fluids. This model is known as the viscous-coupling model (Fourar and Lenormand, 1998):

$$k_{rl} = \frac{S_l^2}{2} (3 - S_l) \quad (16)$$

$$k_{rg} = (1 - S_l)^3 + \frac{3}{2} \mu_r S_l (1 - S_l) (2 - S_l) \quad (17)$$

with  $\mu_r = \mu_g/\mu_l$ . In these experiments in which we flow a liquid and a gas,  $\mu_g$  is much less than  $\mu_l$ , so  $\mu_r$  is very close to zero which means that the second term of Equation 17 can be effectively ignored, which leaves us with the uniform pore-space Brooks-Corey model  $k_{rg}$  equation.

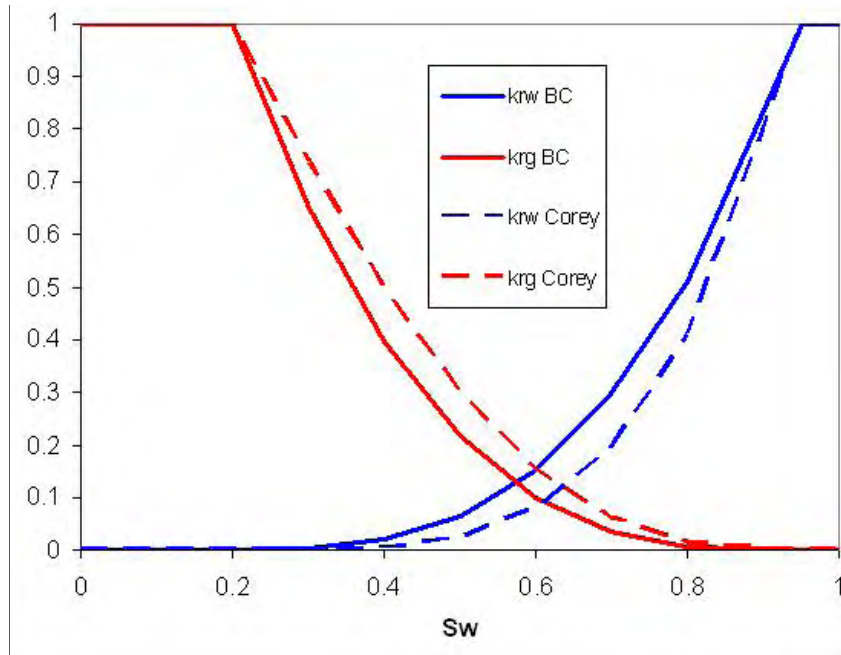


**Figure 1-2. Corey and Brooks-Corey relative permeability models.**

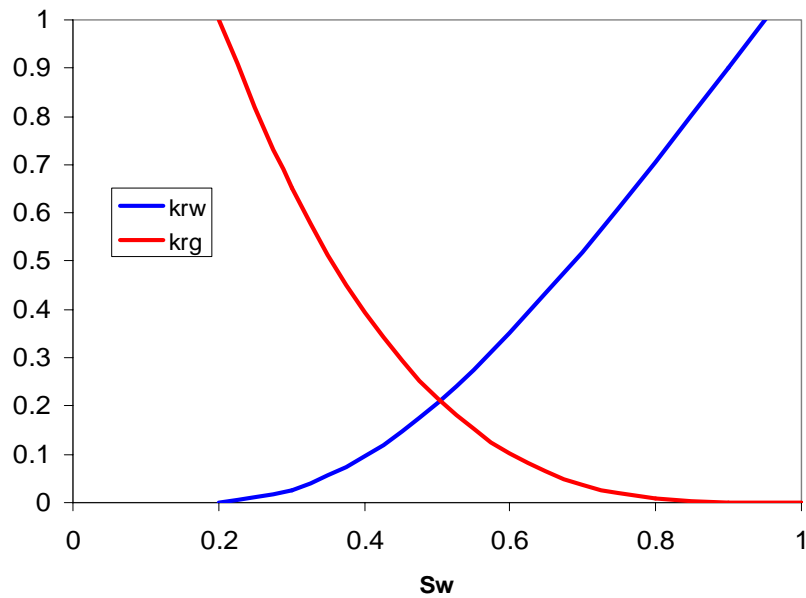


**Figure 1-3. Viscous-coupling relative permeability model.**

## 1.2. Why is Relative Permeability Important?

Traditional single-stage or two-stage flash cycle geothermal power plants rely on steam to drive their turbines. Produced liquid that cannot be flashed to steam is not useful for electricity generation. Therefore, forecasting the amount of steam production as  $S_w$

changes over the life of the reservoir is of critical importance for reservoir planning and management. This is also important for binary plants which only use enthalpy captured from reservoir fluid to provide the energy to drive their turbines. The steam quality has a huge impact on the enthalpy of the fluid that is being brought out of the reservoir, and thus the generation capacity.

With geothermal reservoirs being dominated by fractures, an assumption of X-curve relative permeability behavior has been the common practice in planning of reservoir development. This can lead to significant and expensive errors. For example consider a drawdown of a liquid-dominated reservoir. As the pressure decreases, liquid will boil and  $S_w$  will decrease. If X-curve relative permeabilities are assumed in planning and Corey relative permeabilities are the reality, then one might plan for much more steam production than will occur and will over-invest in a turbine that is much too large (Figure 1-4).

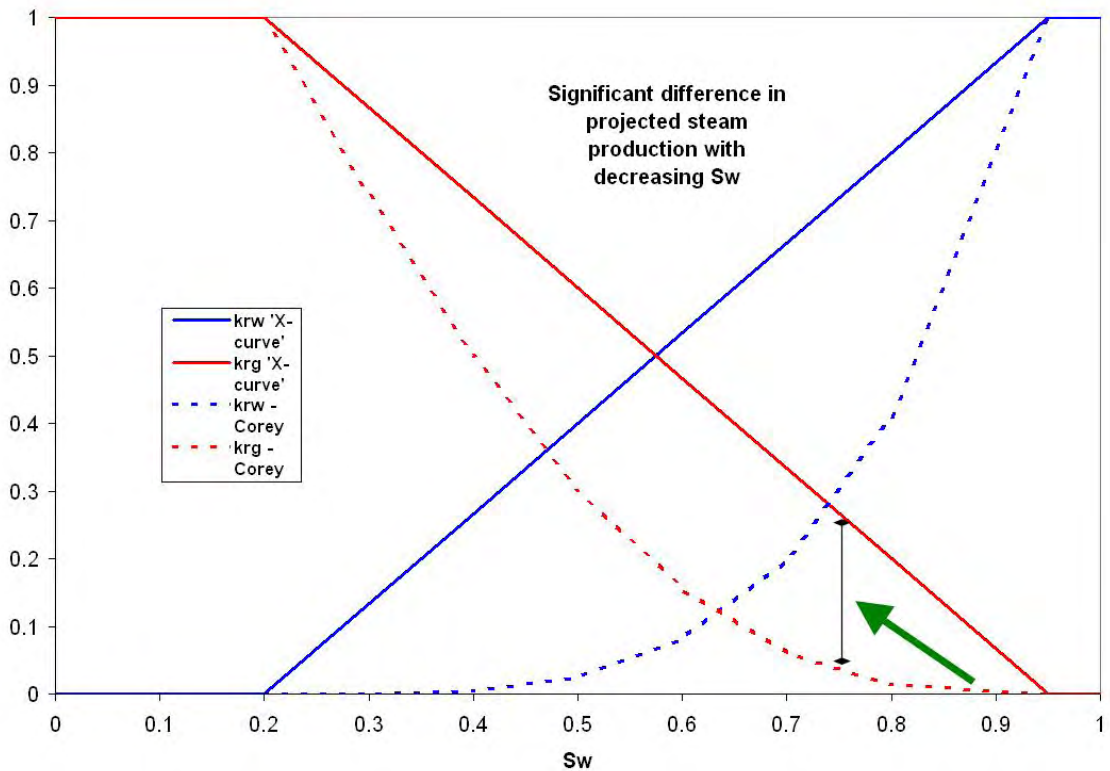


**Figure 1-4. Using an inappropriate relative permeability model can result in expensive overestimations/underestimations of reservoir production capacity over time.**

Relative permeability of CO<sub>2</sub> and water is not important for geothermal applications, but it is equally important for the management of carbon sequestration projects. In order to effectively plan injection of CO<sub>2</sub> into a subterranean reservoir and project its behavior once injected, accurate relative permeability curves are essential.

## Chapter 2

### 2. N<sub>2</sub>-Water and CO<sub>2</sub>-Water Relative Permeability Measurements

This section will first detail the experimental apparatus and methods. Relative permeability measurements will then be presented for both N<sub>2</sub>-water and CO<sub>2</sub>-water relative permeability experiments. Finally, those data will be compared with observations from other studies and with existing relative permeability models. CO<sub>2</sub>-water relative permeabilities were only measured using the smooth-walled fracture.

#### 2.1. Experimental Apparatus

##### 2.1.1. Fracture Apparatus

The fracture used for the experimental measurements was the space between a plate of glass and a flat aluminum surface. It was necessary to have one wall of the fracture be transparent in order to observe flow behavior and measure  $S_w$  visually, as will be described later. The glass surface can be changed to experiment with different textures. For this study, both smooth and homogeneously rough (HR) glass were used. The two plates were held together by an aluminum frame which was mounted vertically. The fracture surface measured 30.48cm x 10.16cm. The fracture aperture was created by a layer of gasket sealant around the edge of the glass for the HR experiments. For the smooth-walled experiments, stainless steel shims with a thickness of 102  $\mu\text{m}$  were used to create the aperture. There were four pressure ports drilled in the aluminum plate for pressure transducer access and two temperature ports (Figure 2-1).

Allan Chen used an optical surface profilometer (OGP; Optical Gaging Product, SmartScope Avant ZIP video measuring system) to determine the surface profile of the HR glass. As shown in Figure 2-2, the HR surface has a repeatable egg-carton pattern with around 160  $\mu\text{m}$  maximum local vertical variation and around 90  $\mu\text{m}$  mean vertical variation. Since the fracture aperture was formed from a layer of gasket sealant, the absolute aperture was still unknown, although the variation was well understood.

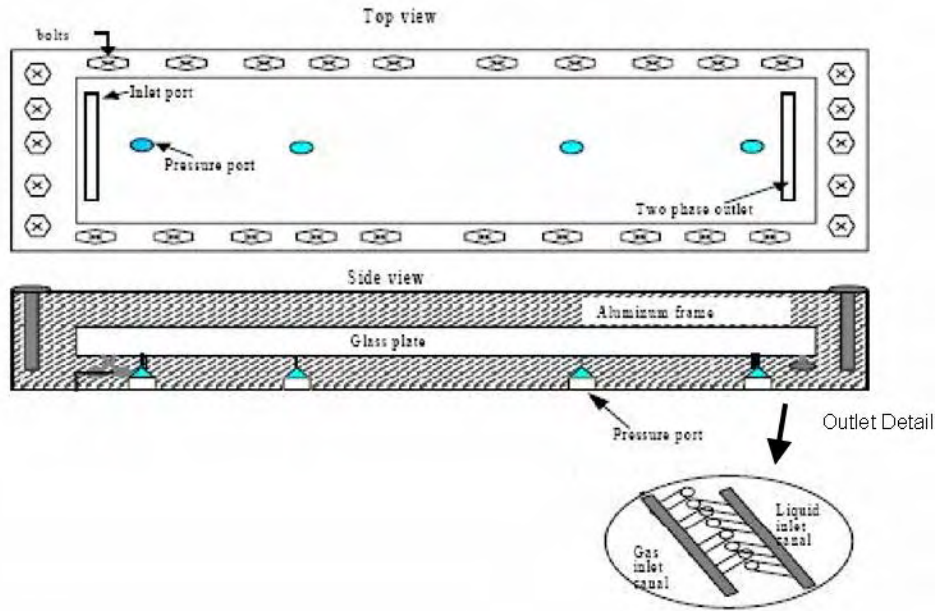


**Figure 2-1. Diagram of fracture apparatus. (Modified from Diomampo, 2001 and Chen, 2005)**

The fluids were injected through a single inlet port into a channel that ran the width of the fracture. The trench served to allow gas and water to separate before they entered the tight fracture aperture. The outlet consisted of 123 alternating holes each with a diameter of 0.51mm. Half of these holes fed into an outlet that exited the top of the fracture and the other half fed an outlet that exited the bottom. Both of the outlets then fed into a single drainage tube. For the rough-walled gas-water experiments, the fracture was oriented the other way around, with a distributed inlet system and a single-point outlet, but that orientation produced significant end effects, so it was reversed for the remainder of the experiments.

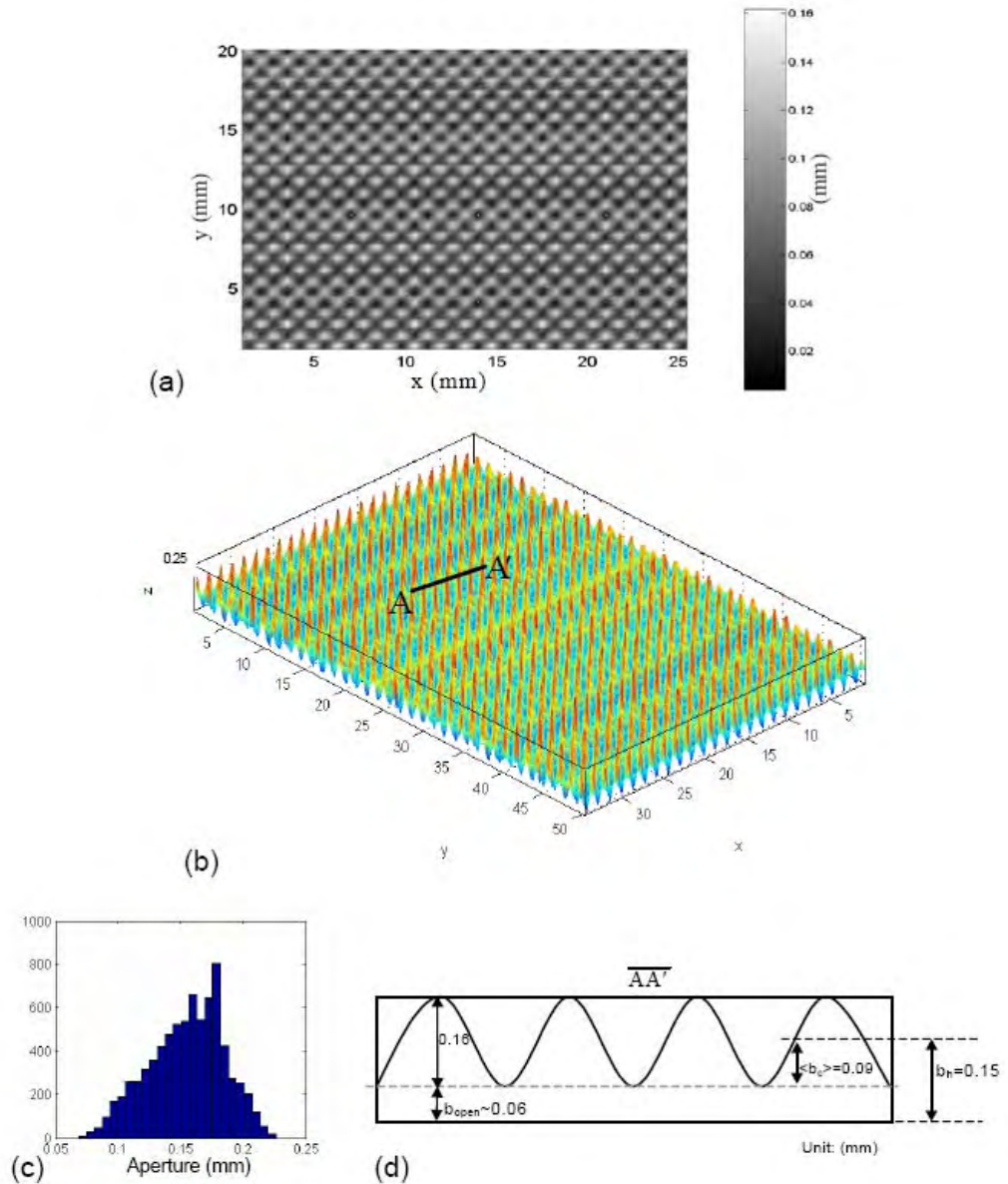


**Figure 2-2. Description of the Homogeneously Rough (HR) glass surface. a) Two-dimensional surface pattern. b) Three-dimensional aperture profile (vertically exaggerated). c) Histogram of aperture distribution. d) Aperture along line A-A'. (Chen 2005)**

The fracture was water-wet, with both aluminum and silica glass having reported contact angles well below  $90^\circ$  (Table 1).

**Table 1. Range of reported static contact angles of water on glass and aluminum.  
(Chen, 2005)**

Material	Water Contact Angle (degrees)
Glass	~0-20
Aluminum	~50-60

Six incandescent light-bulbs were mounted at the top and bottom edges of the fracture to shine light through the glass plate into the fracture. This had the effect of making the two phases in the fracture look very distinct, with the gas phases appearing dark and the water appearing light. This lighting system worked well for saturation measurements, but it had the undesirable effect of increasing the fracture temperature, so it was only turned on for brief periods when saturation measurements were being made. However, even with very limited use, the lighting system caused an upward temperature drift of a few degrees C over the course of a full experiment.

### ***2.1.2. Fluid Injection System***

The water and gas were delivered at individually controlled rates to the fracture apparatus. The deionized water was injected using a Dynamax SD-600 solvent delivery system. Gas injection was controlled through a flow regulator (Brooks Instrument, Flow Meter Model 0151E), which is connected to a mass flow controller (Brooks Instrument, Mass Flow Controller model 5850E, max. rate: 200 ml/min, N<sub>2</sub>). The mass flow controller was designed for N<sub>2</sub> injection, but it was calibrated for CO<sub>2</sub> for use in those experiments as well. The CO<sub>2</sub> maximum flow rate was 78.5% of the N<sub>2</sub> maximum flow rate.

In order to minimize phase change and solution/dissolution within the fracture, the injected gas and water were brought as close to equilibrium as possible before injection. For the N<sub>2</sub>-water experiments, the N<sub>2</sub> was bubbled through water before it was injected so as to increase the moisture content of the gas and prevent water from evaporating inside the fracture. The water was left in an open container for several days to allow for equilibration with atmospheric N<sub>2</sub> and thus prevent gas dissolution inside the fracture.

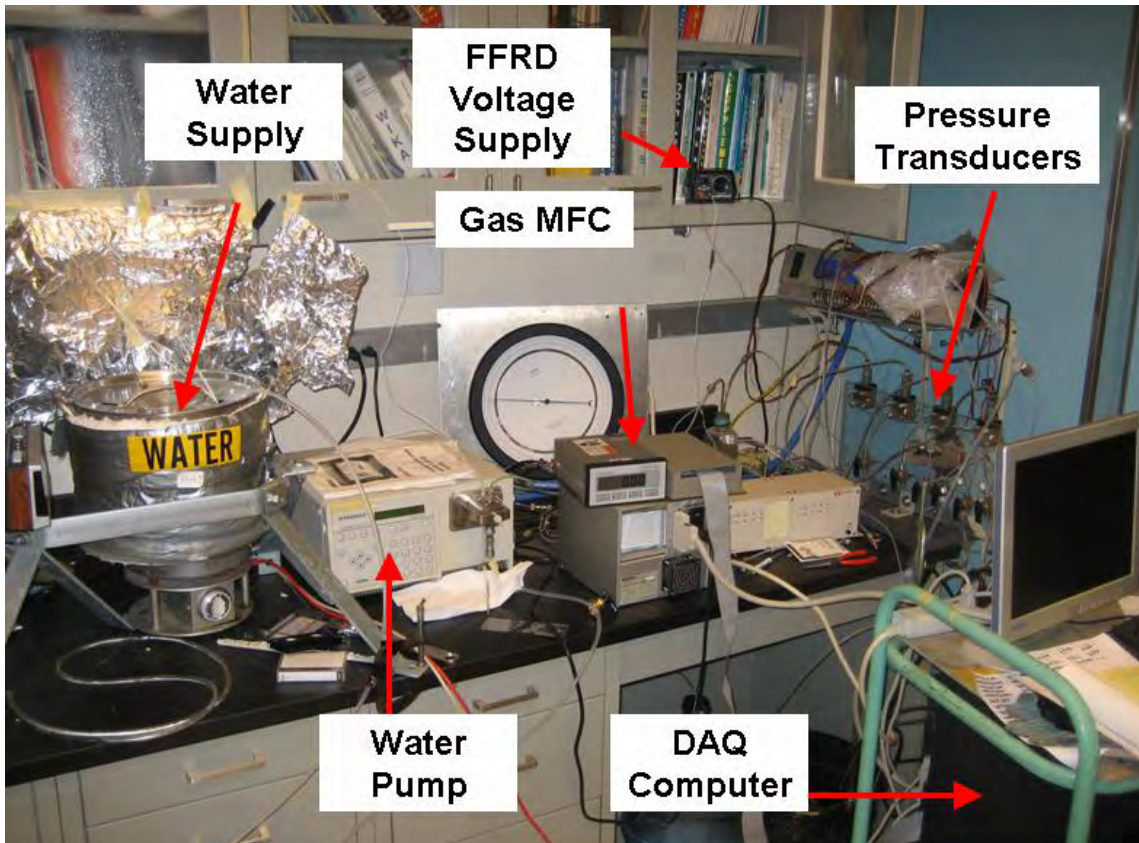


**Figure 2-3. Fluid supply and measurement apparatus.**

For the CO<sub>2</sub>-water experiments, we had to be somewhat more vigilant due to the high solubility of CO<sub>2</sub> in water. The CO<sub>2</sub> was prepared just like the N<sub>2</sub> by bubbling through water. However, the water preparation was more elaborate. First, a vacuum was pulled over the water to bring out as much dissolved gas as possible. Then, the water was bubbled overnight with CO<sub>2</sub>, with the goal being to maximize the amount of CO<sub>2</sub> dissolved in the water before it is injected into the fracture apparatus. In addition, during injection, the water reservoir was bubbled aggressively with CO<sub>2</sub> by periodically putting in pieces of dry ice.

Water injection rates varied from 10 to 0.2 cm<sup>3</sup>/min. Gas injection rates varied from 2.5 to 200 cm<sup>3</sup>/min. All relative permeability measurements were made using gas and liquid viscosities corrected for measured fracture temperature. The viscosity behaviors of CO<sub>2</sub> and N<sub>2</sub> at the temperatures used in the experiment were fairly stable, but the viscosity of liquid water is very susceptible to temperature and must be accounted for (Figure 2-4).

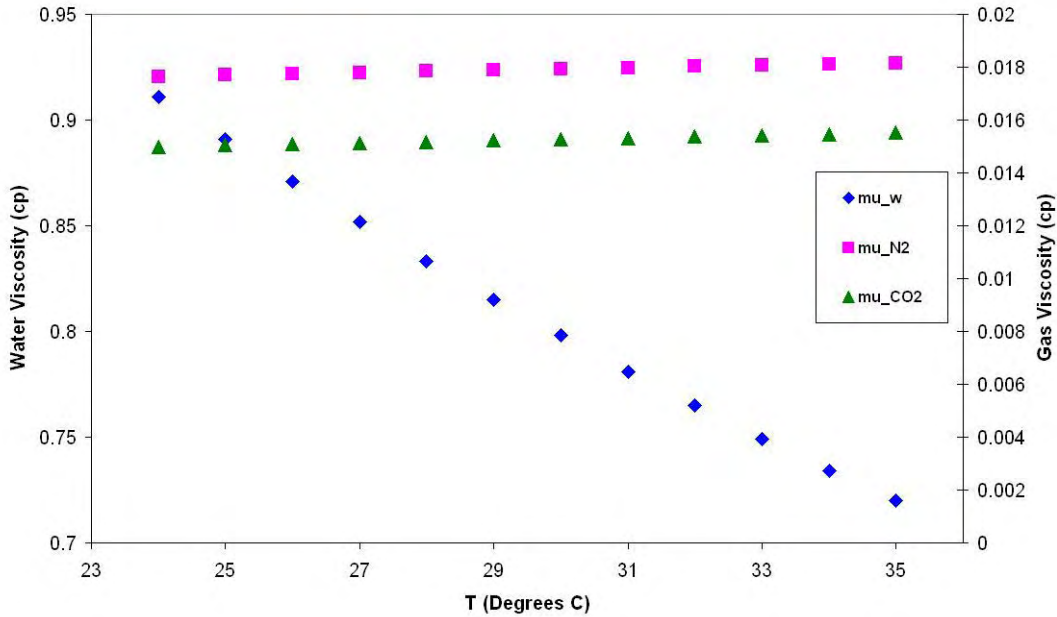


**Figure 2-4. Viscosity behavior of water, CO<sub>2</sub>, and N<sub>2</sub> at temperatures observed during gas-water relative permeability measurements.**

### 2.1.3. Pressure and Temperature Measurements

Low-range differential transducers were used to measure the pressure gradient through the fracture, as well as the intermediate pressure and the two-phase outlet pressure. Two liquid differential transducers (Validyne Transducer, model DP-15, range 0-2 psig) were attached to the four pressure ports inside the fracture to measure the pressure difference through the fracture. One measured the pressure drop across the entire fracture, and the other measured the pressure drop between the middle two pressure ports. Another transducer (Validyne Transducer, model DP-15, range 0-5 psig) was attached to the upstream end of the middle differential transducer. The fourth transducer (Validyne Transducer, model DP-15, range 0-5 psig) was attached at the outlet. These transducers send electrical signals to the data acquisition system, which is monitored, recorded and time-stamped using the LabView® programmable virtual instrument software. Pressure measurements were recorded with a frequency of 5 Hz. A precision pressure gauge was also connected to the fracture outlet for monitoring the fracture pressure when it occasionally climbed above 5 psig.

Temperature measurements needed to be made for the steam-water experiments to be described later, as well as to monitor temperature drift during the gas-water experiments. Temperature measurements were made using T-type thermocouples inserted into two pinhole-sized temperature ports at opposite ends of the aluminum surface of the fracture. Gas-water relative permeabilities were to be measured at room temperature of 24°C, but due to the lighting system necessary to make saturation measurements, the fracture temperature would increase over the course of a day's measurements up to ~31°C, even with only intermittent use. This temperature increase alters the viscosity of both the

water and gas in the fractures, which was accounted for in calculation of relative permeabilities. The temperature measurements were recorded electronically and time-stamped using the same data acquisition system as the pressure measurements and the LabView programmable virtual instrument software. The software recorded the temperature at both temperature ports every 5 seconds.

All measurements were electronic and digitized by using high-speed data acquisition system (DAQ; National Instrument, SCXI-1000 with PCI 6023E A/D board).

#### ***2.1.4. Saturation Measurements***

As mentioned previously, one side of the fracture was made of glass in order to observe flow structures and make saturation measurements. Saturation measurements could perhaps be made using a mass-balance method, but there is no good substitute for visual observation for observing flow behavior inside the fracture. Saturation measurements were made using digital video that was recorded at 30 frames per second. Every 6<sup>th</sup> frame (5 per second) was then extracted from the video and saved as a still image using a Matlab image capture code. These images were time-stamped using the same digital clock that was used to time-stamp the pressure and temperature measurements by placing the monitor displaying the digital time right below the fracture during filming. The images were then captured starting with the first frame of a second (e.g. the first frame of 12:25:34). This was done in order to match saturation measurements with their corresponding relative permeabilities which were calculated with time-stamped pressure measurements.

After the images were captured and time-stamped, they were then cropped to include only the middle third of the fracture surface that was being used to calculate saturation. The rest of the fracture was not observed so as to avoid possible end-effects. After cropping the images were converted to binary black and white images using user-provided training data. The water phase was turned to black and the gas phase was turned to white. Saturation values were then calculated for each image by counting the numbers of black and white pixels. This was all done using a Matlab code. An example is shown in Figure 2-7.

The Matlab codes described here are shown in full in Appendices A-C.

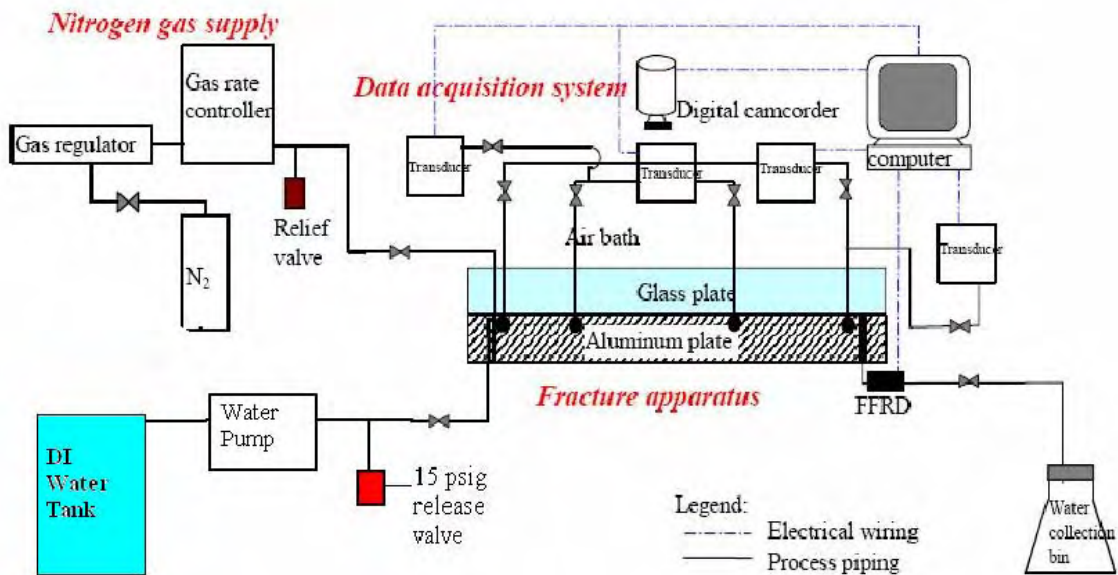


**Figure 2-5. Schematic of experimental apparatus and data acquisition system. (Chen, 2005)**

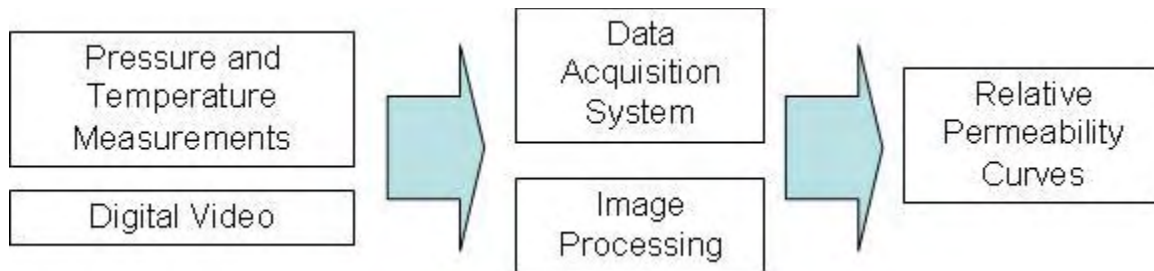


**Figure 2-6. Basic workflow for relative permeability measurements.**

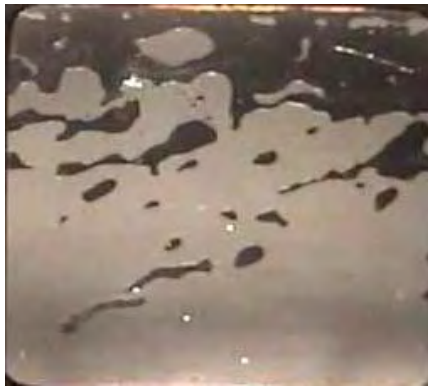


Figure 2-7. Example of saturation value estimation by processing images captured from digital video.

$$S_w = 0.7249$$

## 2.2. Experimental Procedure

### 2.2.1. Fracture Dilation Test

In order to calculate values for  $k_{rw}$  and  $k_{rg}$  from the modified Darcy equations (Equations 3 and 5) we needed to have values for all of the other terms in the equations. The flow rates,  $q_w$  and  $q_g$  were known, the viscosities  $\mu_w$  and  $\mu_g$  were known and tabulated for different temperatures, pressures were measured directly, and saturations were measured and time-stamped with the pressures. The only remaining unknowns were the cross-sectional area  $A$  and the absolute permeability  $k$ . The value for  $A$  could be approximated reasonably well for the smooth-walled experiments because there were virtually no surface variations and the fracture aperture was known. However, for the rough-walled measurements, the fracture aperture was locally variable and impossible to calculate with any precision. The solution to this problem was to lump  $k$  and  $A$  into a single variable  $kA$  which could be measured easily during fully saturated single-phase flow. With the aperture being known for the smooth-walled fracture, it would have been easy to calculate  $k$  explicitly, but calculating  $kA$  served our purposes for calculating relative permeability. Using  $kA$  was also better as a source of comparison with the hydraulic characteristics of the rough-walled fracture.

During experiments, the fracture pressure varied over a range of ~5psi. This pressure variation caused slight dilation and contraction of the fracture aperture, which in turn caused variation in the value of  $kA$ . In order to account for this fluctuation,  $kA$  was measured at several different fracture pressures the morning of each experiment. With this data, a somewhat linear relationship could be determined between fracture pressure and  $kA$  which would be used in calculation of  $k_{rw}$  and  $k_{rg}$  (Figure 2-8).

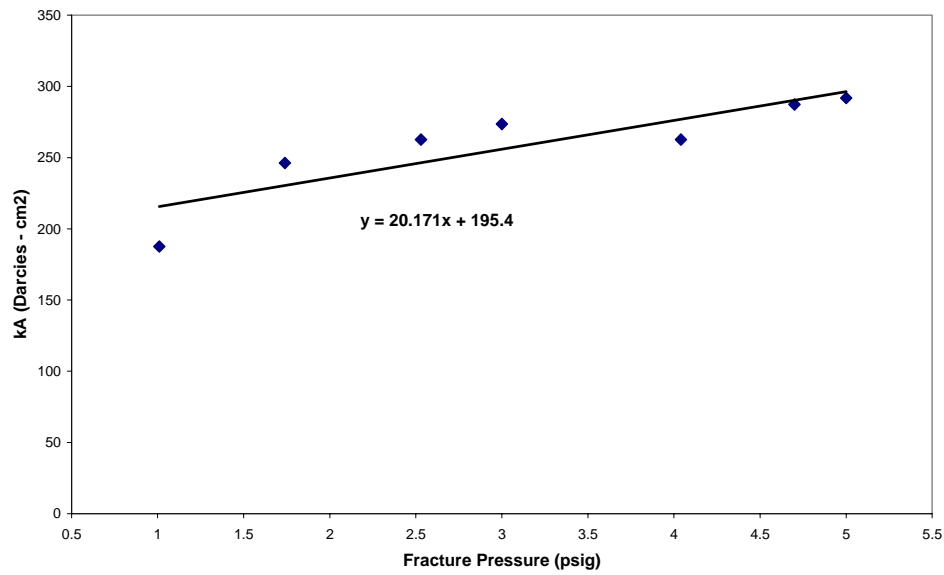


**Figure 2-8. Example of kA behavior with changing fracture pressure.**

### ***2.2.2. Relative Permeability Measurements***

Relative permeability was measured in a series of steady states representing a drainage process. The fracture was initially fully saturated with water using a vacuum pump. Then, with water running through the fracture at a high rate, gas was flowed through the fracture at a low rate until the fracture reached a steady state, which usually took only a few minutes. When steady state was achieved, pressure and temperature measurements were made while video was taken for saturation measurements. The usual length of the video shot for saturation measurements was two minutes. The gas rate was then increased and the process was repeated over several gas/water ratios. When the gas rate had reached its maximum, or the fracture pressure became too high, the water flow rate was lowered along with the gas rate to reproduce the same gas/water ratio, and the gas rate was then incremented again until the minimum water flow rate had been observed with the maximum gas flow rate. Each steady state would produce several hundred data points (5 per second over ~2 minutes).

## **2.3. Results**

### ***2.3.1. Relative Permeability Data***

Due to the inherently unstable nature of the flow, the measured relative permeability values for each flow step could be very noisy, especially when the gas/water ratio was very high or very low and with the smooth-walled fracture. However, the averages from each steady state could be calculated, which produced much more easily discernable

results. However, even these were not the type of clean relative permeability curves that are typically measured on porous core samples (Figure 2-9 to Figure 2-14).

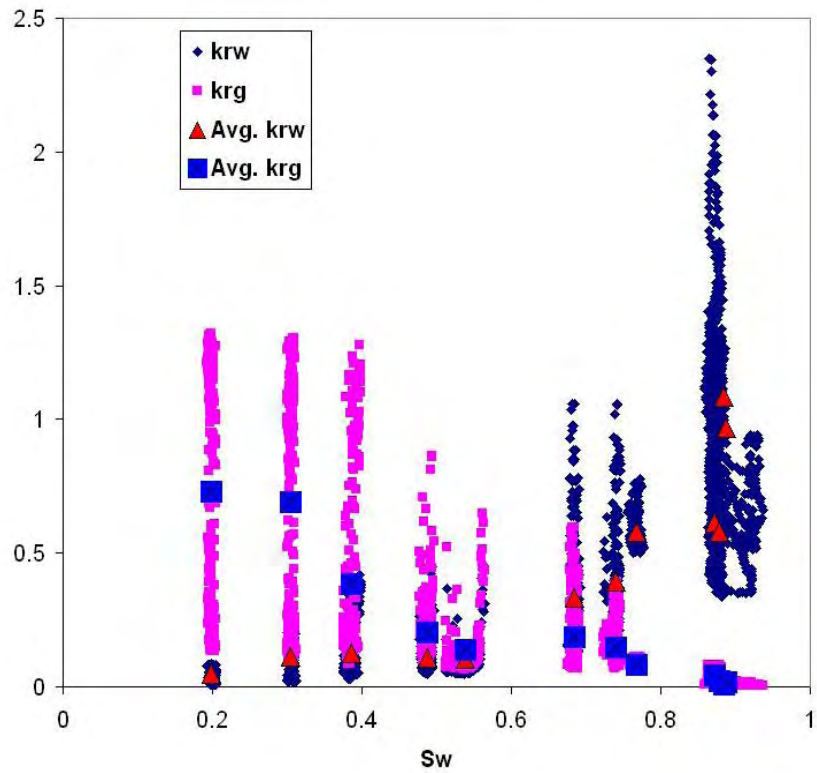


**Figure 2-9. Full and averaged data for CO<sub>2</sub>-water relative permeability in the smooth-walled fracture.**

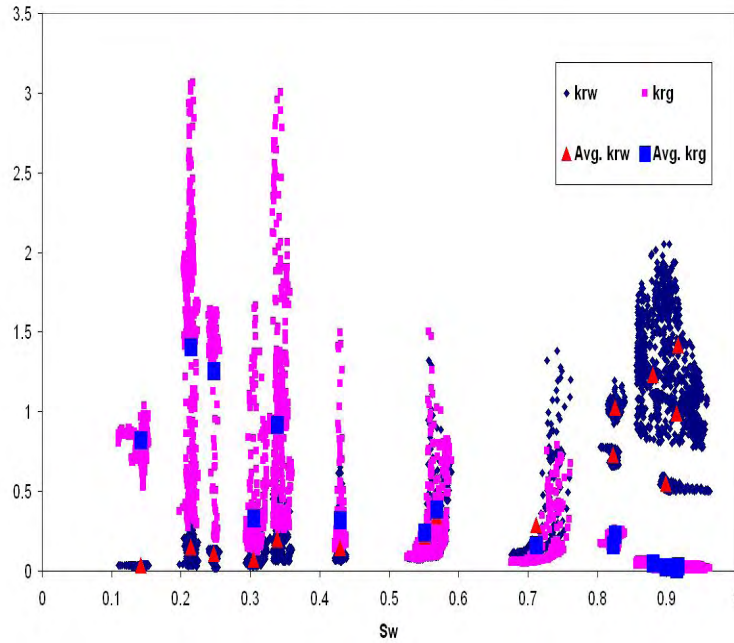


**Figure 2-10. Full relative permeability data from smooth-walled N<sub>2</sub>-water experiments. Average values for each steady state are shown as well.**

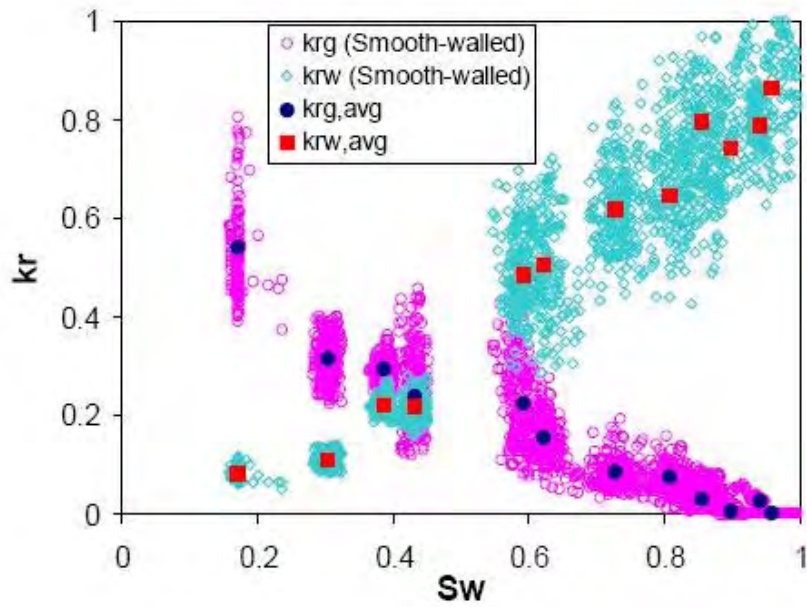


**Figure 2-11. Full and average N<sub>2</sub>-water relative permeability data from Chen (2005) made with the same smooth-walled apparatus oriented horizontally.**

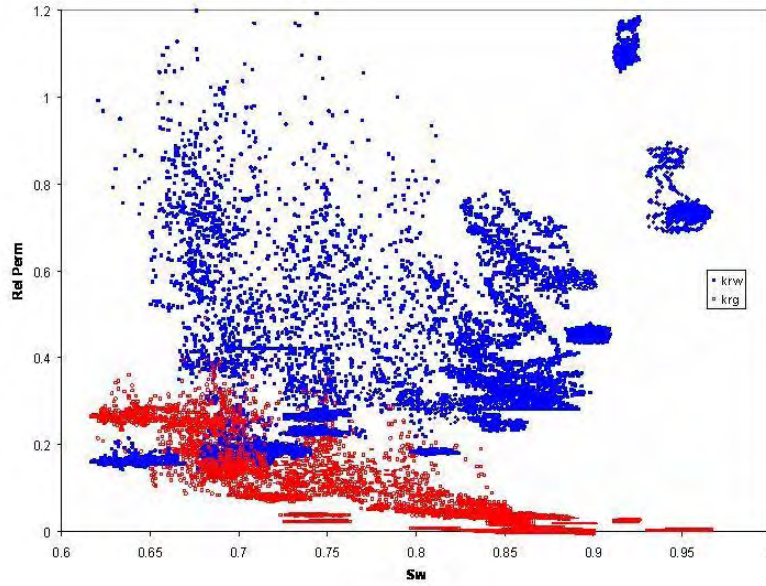


**Figure 2-12. Raw data from N<sub>2</sub>-water relative permeability measurements on the rough-walled fracture. Data are from a single run.**

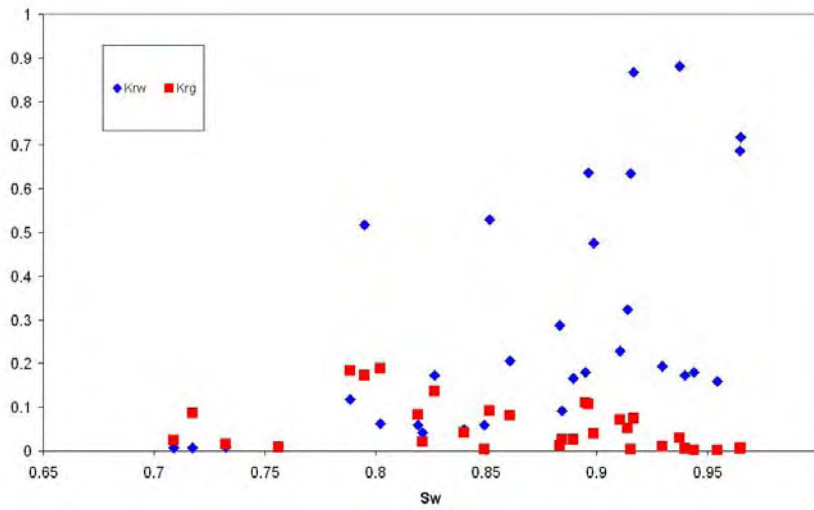


**Figure 2-13. Averaged N<sub>2</sub>-water relative permeability data from the rough-walled fracture. Averaged data are from multiple runs.**

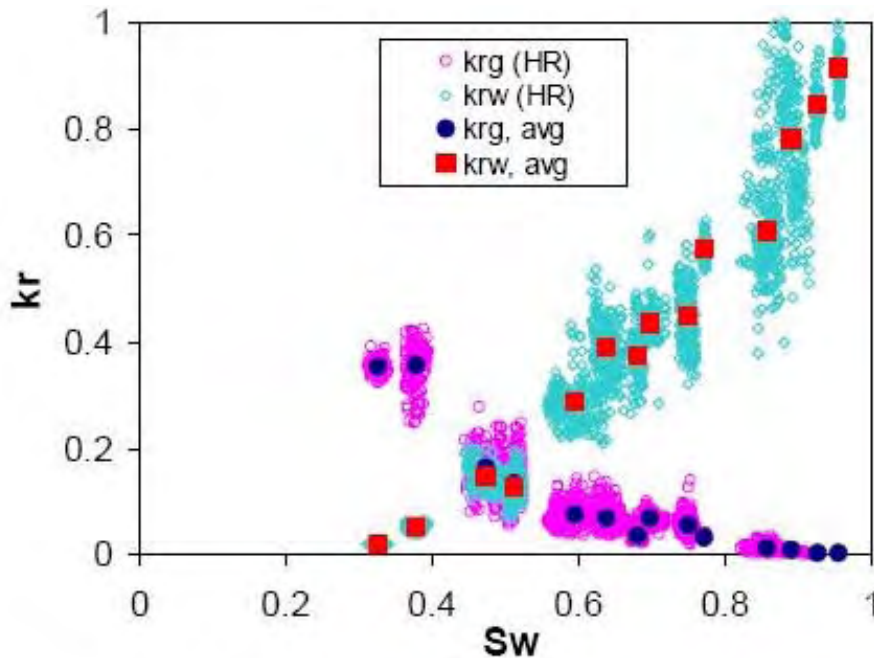


**Figure 2-14. Full and average N<sub>2</sub>-water relative permeability data from Chen (2005) made with the same rough-walled apparatus oriented horizontally.**

### 2.3.2. Smooth-Walled Observations

The flow patterns observed during gas-water flow in the vertical fractures with the smooth-walled apparatus were virtually identical for the CO<sub>2</sub>-water and the N<sub>2</sub>-water relative permeability measurements. Starting with the fracture 100% saturated with water, a gas channel would form along the top edge of the fracture. If  $q_g$  was especially low, the channel would open and close periodically. As the gas/water ratio increased, the gas channel became permanent and grew in size with increasing gas/water ratio until only a small channel of water remained along the bottom edge of the fracture (Figure 2-15).

The two-phase flow was not entirely steady though. The gas-water interface was not straight; it would bend and meander in a seemingly random manner. The relative width of the gas and water channels would increase and decrease periodically.

There were two clear differences between the CO<sub>2</sub> and the N<sub>2</sub> relative permeability behavior. The first was that the residual saturation was higher with CO<sub>2</sub> than it was with N<sub>2</sub>. This may be the result of the higher solubility of CO<sub>2</sub> in water. Instead of pushing the water out of the fracture, the CO<sub>2</sub> dissolved into the water. It could also be because due to equipment limitations, the maximum CO<sub>2</sub> flow rate was only 78.5% of the maximum N<sub>2</sub> flow rate. The other difference was that residual gas saturation was virtually zero with the CO<sub>2</sub>. With the N<sub>2</sub>, it was always very difficult to rid the fracture of all gas bubbles before an experiment, even when using a vacuum pump. With the CO<sub>2</sub>, there would initially be a few residual bubbles, but they would usually dissolve away fairly quickly.

Another observation made when comparing the CO<sub>2</sub> and N<sub>2</sub> relative permeability curves was that the N<sub>2</sub> curve went higher compared to its corresponding water curve than CO<sub>2</sub> went compared to its own water curve. In other words, were both sets of relative permeability data to be normalized to 1, the maximum N<sub>2</sub> relative permeability would be greater than the CO<sub>2</sub> maximum.

Chen (2005) did not experiment with CO<sub>2</sub>, so there is no direct comparison of results to be made in that regard. His results for the N<sub>2</sub>-water relative permeability measurements for the same fracture oriented horizontally were similar in shape, although different in magnitude. The magnitude difference can be attributed to errors in measurement of  $kA$  which will be described later in Section 2.4.

### **2.3.3. Rough-Walled Observations**

Using the rough-walled fracture, the tendency was for the gas to form a channel along the top edge of the fracture, but this was not as clearly defined as with the smooth walled fracture. Layered flow was observed with very low gas flow rates. Once  $q_g$  increased past  $\sim 20$  cm<sup>3</sup>/min, the gas flowed through stable subhorizontal tortuous channels near the top of the fracture in addition to flowing along the top edge. As  $q_g$  increased further, the downward infiltration of gas channels continued until two-phase flow was occurring in the top third of the fracture. The bottom half of the fracture was not infiltrated by gas at all until  $q_g=200$  cm<sup>3</sup>/min, at which point a periodic gas channel would form and dissipate across the bottom edge of the fracture. The channels were very stable with low flow rates, but became more dynamic and even turbulent, exhibiting slug flow with higher  $q_g/q_w$  coupled with high overall flow rates. One very interesting characteristic of N<sub>2</sub>-water flow in the rough-walled fracture was the very high value for residual water saturation  $S_{rw}$ . With maximum  $q_g$  and  $q_w=0$ , the minimum saturation obtained was  $\sim 0.6$ . Chen measured  $S_{rw}$  to be 0.25 on the exact same apparatus oriented horizontally.

Although the data from the vertical rough-walled fracture was noisy (Figure 2-12), the general shape of the curves seems to be very similar to that measured by Chen on the same apparatus oriented horizontally.

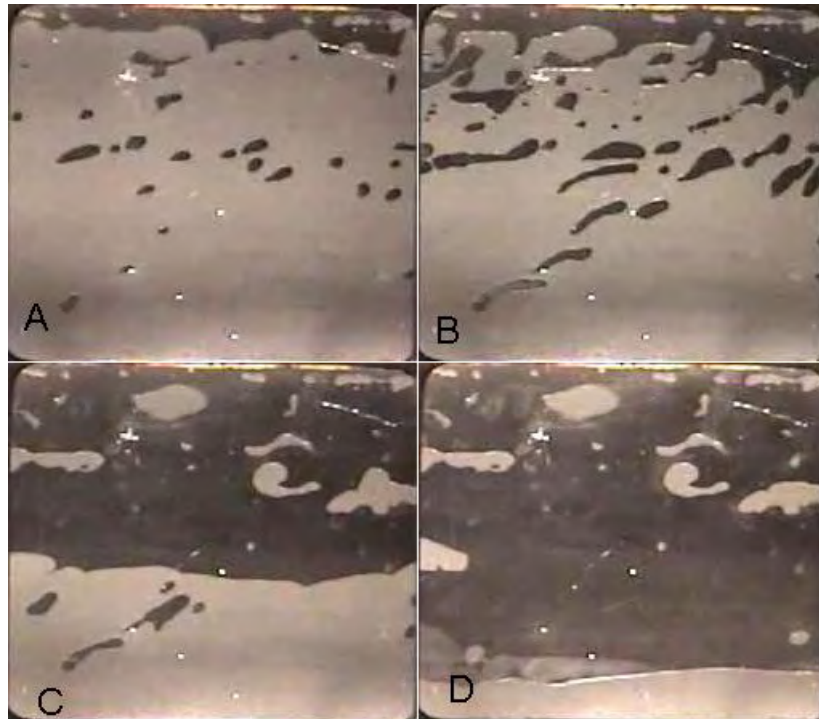


**Figure 2-15. CO<sub>2</sub>-water flow structures in the smooth-walled fracture with gas-water flow ratios increasing A-D. Flow structures were identical for N<sub>2</sub> and CO<sub>2</sub>. The dark phase is gas and the light phase is water.**

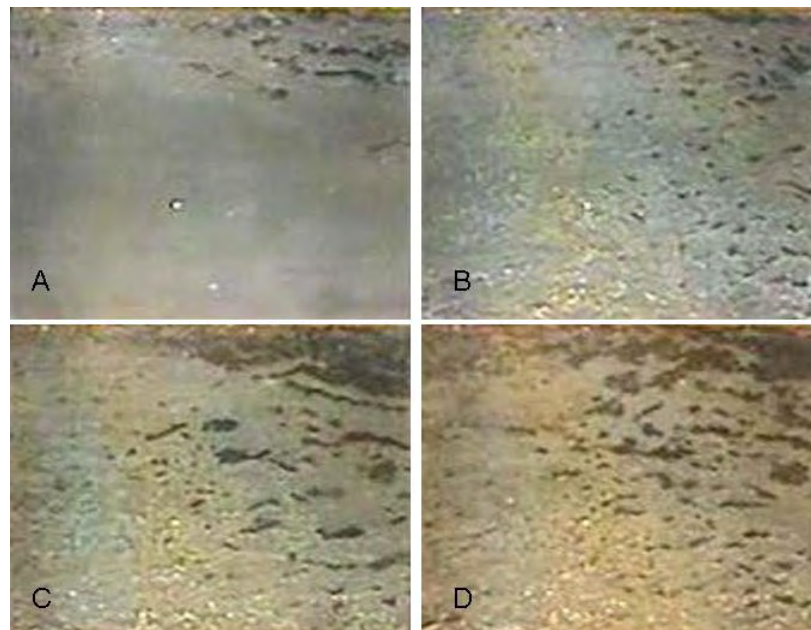


**Figure 2-16. N<sub>2</sub>-water flow structures in the rough-walled fracture with gas-water flow ratios increasing A-D. The color difference is the result of a changed camera setting half-way through the run. The dark phase is gas and the light phase is water.**

## 2.4. Discussion

There are a few characteristics that are immediately evident upon inspection of the relative permeability curves from the N<sub>2</sub>-water experiments. There is a great deal of noise and variation in the data, even when averaged. This is in part due to the design and orientation of the fracture apparatus. As described earlier, both the water and gas are injected at fixed volumetric rates regardless of pressure. The two phases are then mixed at a T-junction and then they flow into the single phase inlet of the fracture. Ideally, the two phases would mix evenly at the T-junction and form regular gas and water slugs, but what often happened was that only one phase would flow for a period up to ~30 seconds until the other phase built up enough pressure to dominate the flow. The result was that sometimes instead of injecting mixed gas and water, we injected alternating gas and water. Over time, the flow rates were still constant, but the short term flow ratios were difficult to maintain.

The transitions from one phase flowing to the other could cause artificial noise in the pressure measurements which were used to directly calculate relative permeability; especially at very high or very low gas/water ratios. This is because the pressure drop over the fracture was measured down the middle of the fracture as dictated by the location of the pressure ports (Figure 2-1). As mentioned previously, the gas would form a separate channel above the water. Due to the alternating flow effect, if only gas was flowing and the gas channel did not pass over both of the pressure ports, zero or even negative values could be measured for  $\Delta p$ . This is because only gas was flowing at that moment and thus the water pressure gradient was zero. The same thing happened with the water phase. These occurrences were filtered out of the raw data, but so as to not eliminate any 'true' data, the filter was very liberal in deciding which data to keep, which results in a great deal of noise in the data.

As mentioned previously the fracture was oriented the other way around for the rough-walled experiments. This did not have the alternating flow problem, but instead produced significant and disruptive end effects. The single-phase outlet was located in the bottom half of the fracture which caused significant downward deviation of the gas channels from their natural path. For future experiments with a similar apparatus, we would recommend distributing both the inlet and the outlet so as to eliminate these kinds of problems.

Another characteristic that was immediately apparent when inspecting the relative permeability data, especially from the N<sub>2</sub>-water experiments on the smooth-walled fracture, was that there were some relative permeability values measured that were greater than 1, which should be impossible. The more extreme deviations (those relative permeability values that are greater than ~2) can be attributed to the noise. However, even the average values are above 1 in some cases which means that there was a more systemic phenomenon occurring.

As mentioned previously, the  $kA$  value was measured before each run of the experiment. These measurements were made with the fracture 100% saturated with water, but it is possible that some of the tiny distributed outlet ports were blocked with air bubbles, which sometimes happens. These bubbles usually cleared once gas and water were flowed at the same time. This would have caused the value measured for  $kA$  to be lower than it actually was, and thus result in the elevated relative permeability values that were calculated. This hypothesis is reinforced by the fact that the CO<sub>2</sub>-water average relative permeabilities almost all stay below 1. Any residual CO<sub>2</sub> bubbles very quickly dissolved into the water, so it is very unlikely that any residual CO<sub>2</sub> would be blocking the outlet ports. The elevated values are not of critical importance though, because it is the shape of the curves that defines the relative permeability behavior.

The difference in  $S_{rw}$  between the fracture oriented vertically and horizontally is very interesting. If a reservoir is known to have many vertical fractures, the high  $S_{rw}$  can have real impacts on reservoir management. Increasing fracture roughness also has the effect of increasing  $S_{rw}$ , but this is what would be expected.

## **2.5. Comparison with Established Relative Permeability Models**

### ***2.5.1. Smooth-Walled Fracture***

Although the flow through the fracture was mostly laminar, the measured relative permeabilities are not X-curves. This means that even the small amount of interference at the liquid-gas interface and surrounding a few small pockets of water in the gas channel were enough to cause significant deviation from the X-curve.

Although the magnitudes of the CO<sub>2</sub> and N<sub>2</sub> relative permeability curves were different, which can be attributed to the  $kA$  values used to calculate them, the shapes of the curves were very similar. The only real differences were the  $S_{rw}$  was higher for the CO<sub>2</sub> measurements for the suspected reasons discussed above and the maximum relative permeability of CO<sub>2</sub> was less than that of N<sub>2</sub>.

The average measured relative permeability values were normalized to 1 and plotted with X-curves and Corey curves (Figure 2-17, Figure 2-18). Both curves show Corey-like behavior at high phase saturations. However, at intermediate-to-low phase saturations, the relative permeabilities that were measured were consistently higher than the Corey relative permeability curve. At very low phase saturations (the last 10% before  $S_{wr}$  or  $S_{gi}$  was reached) the measured data appears to follow X-curve relative permeabilities.

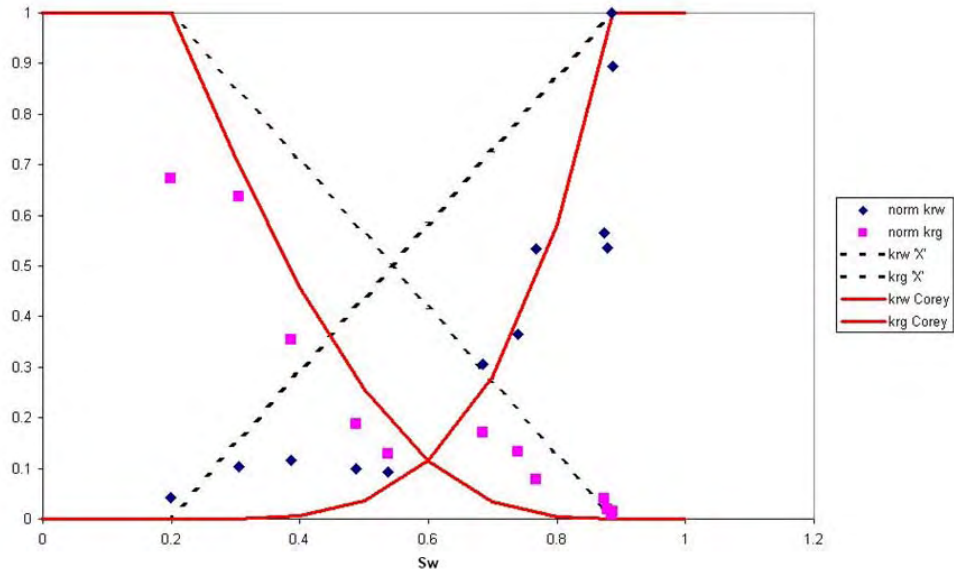


**Figure 2-17. Normalized CO<sub>2</sub>-water average relative permeability measurements compared with the X-curve and Corey-type curves.**

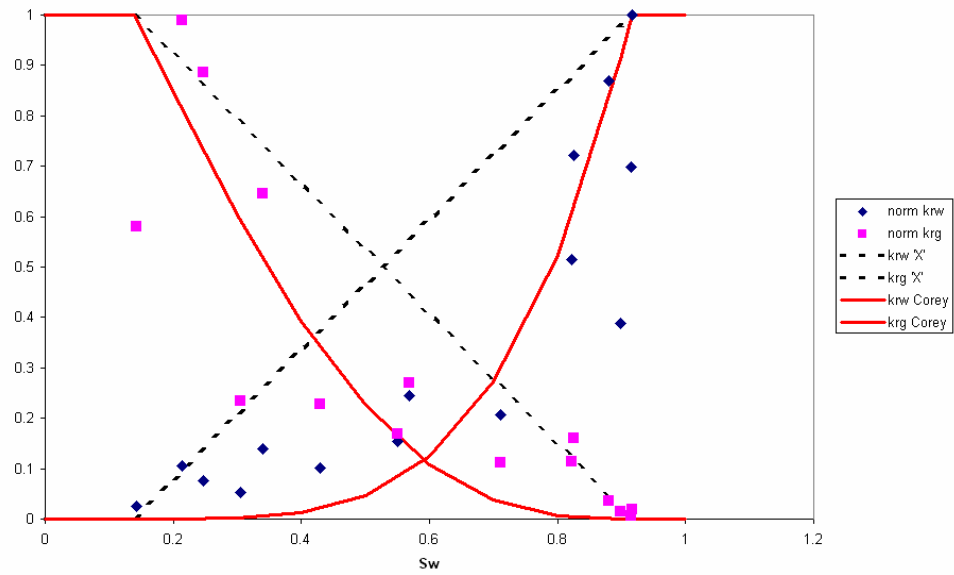


**Figure 2-18. Normalized N<sub>2</sub>-water average relative permeability measurements compared with the X-curve and Corey-type curves.**

### 2.5.2. Rough-Walled Fracture

The rough-walled fracture average data was compiled and compared with various relative permeability models. As could be expected with data this noisy, no existing model represents the experimental data very well. However, comparison does shine some light on a few trends. First, the X-curve is not valid here. Most of the data support a relative permeability model with very high phase interference at intermediate saturations. Second, the magnitudes of the gas relative permeability are significantly smaller than the water relative permeability.

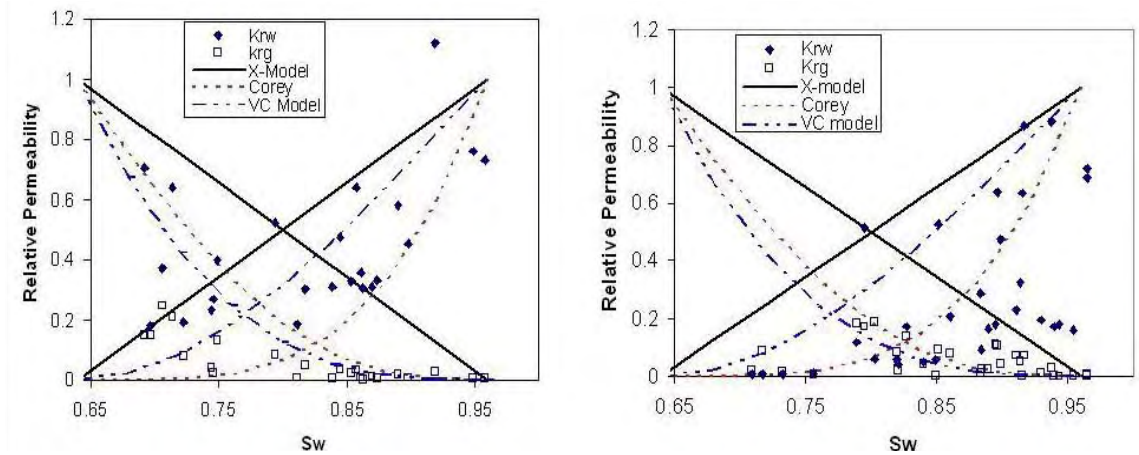


**Figure 2-19. Averaged N<sub>2</sub>-water relative permeability data from two different runs compared with various known relative permeability models.**

## Chapter 3

### 3. Steam-Water Relative Permeability Measurements

Understanding gas-water relative permeabilities in vertical fractures is important, but in order to obtain a relative permeability model that can be applied directly to geothermal reservoirs, steam-water relative permeability must be measured. This is a more complicated process than gas-water relative permeabilities because it is physically impossible to eliminate phase transformation effects within the apparatus at saturated conditions. This necessitated the alteration of the experimental apparatus and procedure.

#### 3.1. Experimental Apparatus

The experimental apparatus from the gas-water experiments had to be modified to accommodate measurement of steam-water relative permeabilities. The most significant modification was the placement of the entire apparatus in a temperature-controlled air-bath that could bring the entire system up to boiling temperatures. The air-bath had a window through which saturation measurements could still be made with digital video.

In order to measure relative permeabilities, it was necessary to deliver known amounts of steam and water to the fracture. This presented two options. One method was to generate the steam outside the apparatus and inject it separately as was done with  $N_2$  and  $CO_2$ . This was troublesome because even if we injected steam at a known volumetric rate, phase transformation effects would make that rate meaningless for relative permeability measurement. Instead, we opted to inject water at a known volumetric rate as was done in the gas-water experiments, except we ran the water through a ~6ft heating coil inside the air-bath to generate steam from the injected water and thus have steam-water equilibrium at injection. Because the entire fracture was at saturated conditions, steam-water phase changes continued inside the fracture.

In order to ensure only two phases (water and steam) were present in the fracture, the injection water had to be completely deaerated. First, regular deionized water had vacuum pulled over the surface of the water for several hours or overnight. The water was then boiled as it was pumped to minimize the presence of any dissolved gases in the injection fluid. The water was run through a series of cooling tanks before reaching pump to keep from doing any damage to the pump machinery which was not specified to tolerate high temperatures.

### ***3.1.1. FFRD Apparatus***

The chosen injection scheme allowed for the existence of steam-water equilibrium within the fracture, but it did not allow for direct measurement of the flow rates at the inlet. However, the outlet flow rates could be determined if fractional flow was known at the outlet.

An optical Fractional Flow Ratio Detector (FFRD) was used, slightly modified from the design of Alan Chen (2005). The principle behind the FFRD is that steam and water flowing through a length of tubing will allow different amounts of light to pass through. We took advantage of that property by mounting a phototransistor (NTE 3036, NPN-Si, visible) and a small LED bulb on opposite sides of the outlet tubing as close to the end of the fracture as possible. The entire FFRD was mounted inside a rubber stopper with transparent nylon tubing passing through the middle and the LED and phototransistor mounted in opposite sides. When connected to a voltage, a phototransistor would modify the voltage signal it transmits based on how much light it is exposed to. The phototransistor was attached to a voltage source and connected to the data acquisition system which recorded the voltage signal at 250-500 Hz, with higher frequencies being used to measure higher flow rates.

The outlet tubing was thin enough that purely slug flow took place featuring alternating pure water and pure steam with the exception of a very small meniscus at each interface. When very high steam flow rates (greater than ~200 cc/min) were coupled with low water rates (less than 2 cc/min) the slug flow regime broke down and only small droplets of liquid water could be seen moving very rapidly through the outlet tubing. When slug flow broke down it became necessary to increase the frequency with which the voltage signal was recorded because otherwise some water signals would be missed. Even with high measurement frequency, the data became increasingly difficult to decipher as steam/water ratios reached larger and larger values.

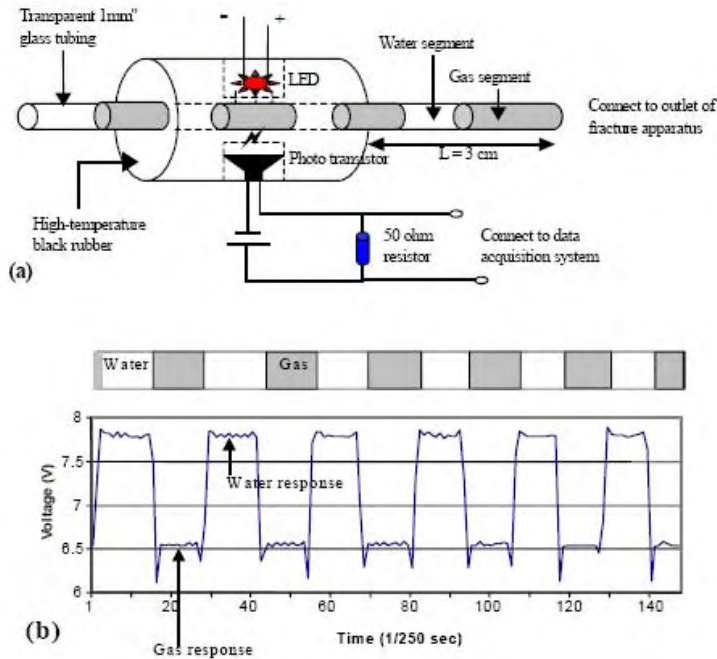


**Figure 3-1. a) Schematic of FFRD device. b) Example of water and gas FFRD signals corresponding to actual flow (Chen 2005).**

After the FFRD data was recorded, a histogram of all of the recorded voltages was created. The FFRD histogram was bimodal in nature, with a peak for the water response and valley for the gas response with very few data in between, as can be seen in Figure 3-1b. After examining the histogram and determining where the water and gas signal peaks were, a threshold voltage was designated as the voltage at which the fewest number of signals were recorded; in other words the lowest point on the histogram between the two peaks. A sample histogram can be seen in Figure 3-2.

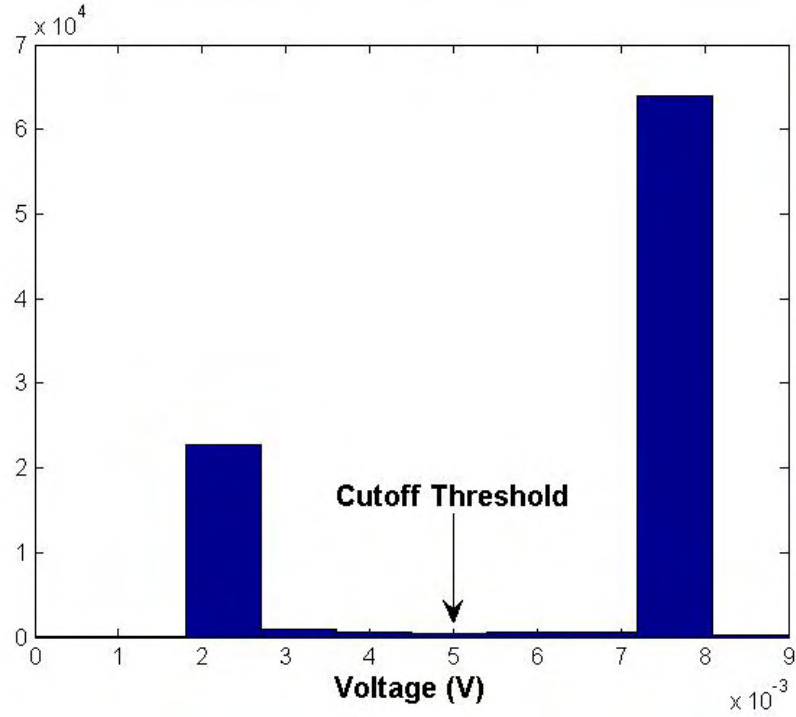


**Figure 3-2. Sample histogram from FFRD data.**

Finally, once the threshold value was designated, the fractional flow was calculated as follows:

$$f_w = \frac{N_w}{N_w + N_g} \quad (18)$$

$$f_g = \frac{N_g}{N_w + N_g} \quad (19)$$

with  $f_w$  and  $f_g$  being the fractional flows of water and gas, and  $N_w$  and  $N_g$  being the number of recorded water and gas signals, respectively. With the fractional flows known as well as the mass flow rate known from the fixed water input rate, the volumetric flow rates could be calculated by using a mass balance method and the definition of fractional flow:

$$m_{in} = q_{out,t}(\rho_w f_w + \rho_s f_s) \quad (20)$$

$$f_w = \frac{q_{out,w}}{q_{out,t}} \quad (21)$$

$$f_g = \frac{q_{out,g}}{q_{out,t}} \quad (22)$$

with  $m_{in}$  being the input mass flow rate,  $q_{out,t}$  being the total outlet volumetric flow rate, and  $\rho_w$  and  $\rho_g$ , and  $q_{out,w}$  and  $q_{out,g}$ , being the densities and volumetric flow rates of water and gas, respectively. We can then solve for the volumetric flow rates of water and gas:

$$q_{out,w} = f_w \frac{m_{in}}{f_w \rho_w + f_g \rho_g} \quad (23)$$

$$q_{out,g} = f_g \frac{m_{in}}{f_w \rho_w + f_g \rho_g} \quad (24)$$

The FFRD was calibrated during gas-water flow when actual volumetric flow rates of each phase were known and a satisfactory correlation was observed as seen in Figure 3-3.

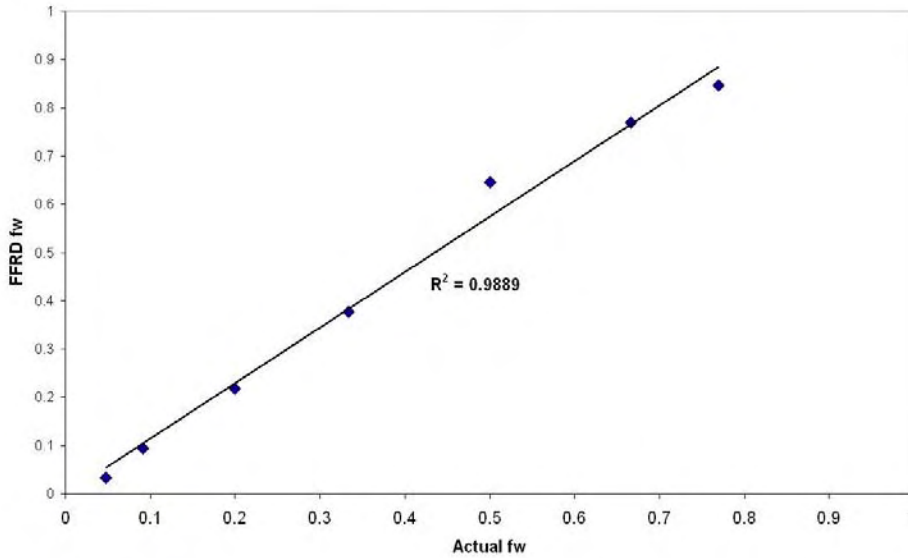


**Figure 3-3. Calibration of the FFRD with known fractional flows.**

### 3.1.2. Pressure Measurements

Pressure measurements were made with the same transducers in the same configuration as in the gas-water experiments. However, the water in the pressure tubing connecting the pressure ports in the fracture to the transducers had a tendency to boil when the apparatus was at elevated temperatures. This disrupted pressure measurements

significantly. To rectify the boiling problem, cooling water was circulated over the pressure tubing to keep steam from forming within the tubing. A rough schematic of the pressure tubing cooling system is shown in Figure 3-4.

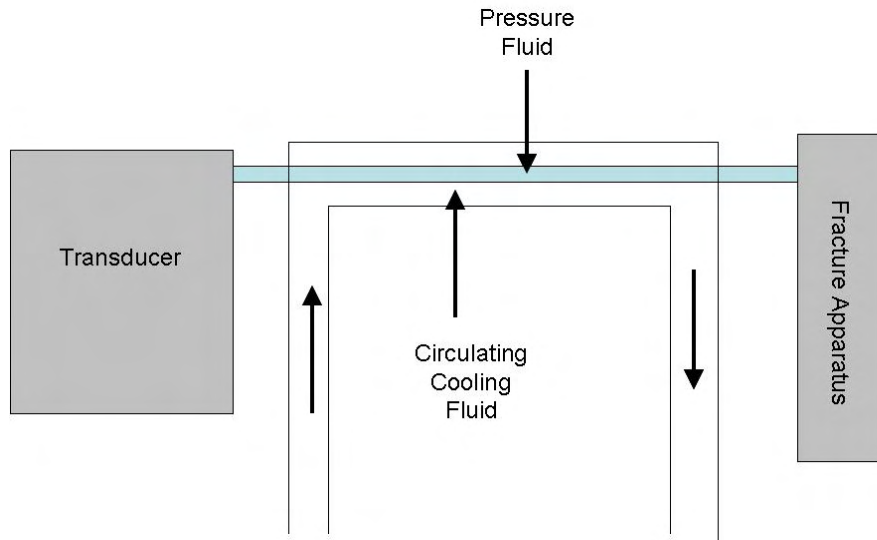


**Figure 3-4. Diagram illustrating the system for keeping the fluid in the pressure tubing cool.**

### ***3.1.3. Back-Pressure Apparatus***

A back-pressure apparatus was attached to the outlet of the fracture so as to modify the absolute fracture pressure as the experiment was running. The back-pressure apparatus consisted of a length of tubing running into a funnel suspended at a fixed height. The funnel then drained into a wastewater container. The pressure head created by fixing the funnel at various heights translated directly into the fracture. The apparatus allowed for up to 3.4 meters of variable hydraulic head to be applied to the outlet of the fracture (Figure 3-5).

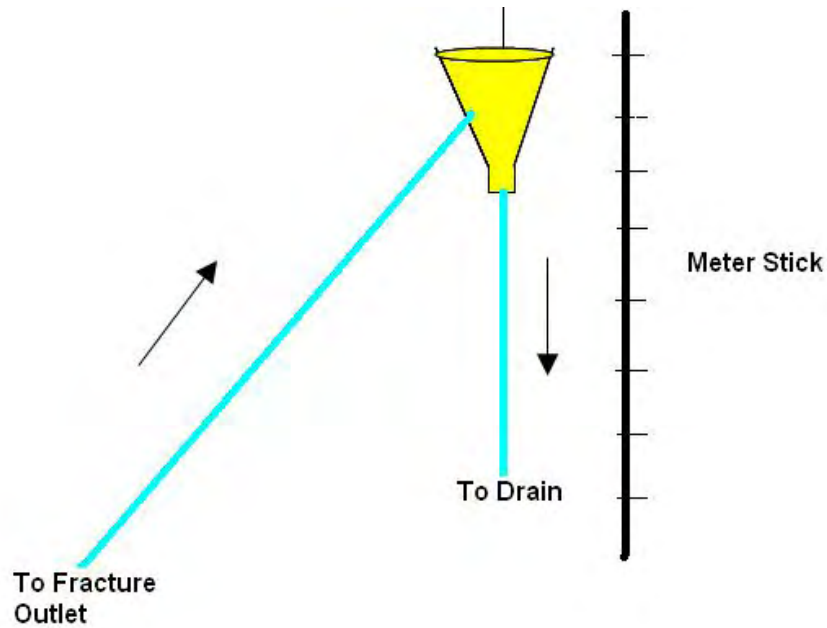


**Figure 3-5. Schematic of the back-pressure apparatus used in the steam-water experiments.**

### 3.2. Procedure

The procedure for measuring steam-water relative permeability was only slightly different from that used for that used in measuring  $N_2$ -water or  $CO_2$ -water relative permeabilities. The goal was still to measure relative permeabilities in a drainage process, creating a series of steady states with decreasing  $S_w$ .

After the entire apparatus had been brought to a steady temperature of around  $105^\circ C$ , water was flowed through the fracture at a fixed rate. The back-pressure was kept as high as possible so as to minimize steam formation. This state was recorded and measured for relative permeability measurement. The back pressure device was then lowered, thus reducing fracture pressure and allowing more steam to form and increasing the steam-water flow ratio. This was allowed to flow until steady state was achieved (~30-45 minutes) and was then recorded. This procedure was repeated until the fracture pressure could not be lowered any further. At this point, if a higher steam/water ratio was still desired, the water input rate could be lowered, which in turn lowered the fracture pressure. This facilitated an even higher steam-water ratio. The steam water experiment was performed on both smooth and rough walled fractures. Due to the elevated temperature and rapid circulation of air in the oven, the lighting did not affect the fracture temperature more than 1 or 2 degrees over the course of the day, although this was still corrected for when calculating relative permeability.

### 3.3. Results

#### 3.3.1. Smooth-Walled Relative Permeability Results

For the smooth-walled fracture, the measured steam-water relative permeability curves have similar characteristics to those measured for gas-water flow. There is significant noise in the data, and there were steam relative permeability values measured that are greater than 1. In terms of the curve characteristics, there is clearly significant phase interference in steam-water flow in vertical fractures. The steam relative permeability curve is significantly steeper than the  $N_2$  or  $CO_2$  curves.

This phenomenon could be a result of phase transformation effects. By phase transformation effects we mean that in addition to the steam physically pushing water through the fracture and vice versa, the steam moves through the fracture on a small scale by evaporating water at the downstream end of the pressure gradient and condensing at the upstream end. With this mechanism, the mass flow can be negligible, but the steam bubble will still move (Figure 3-6).

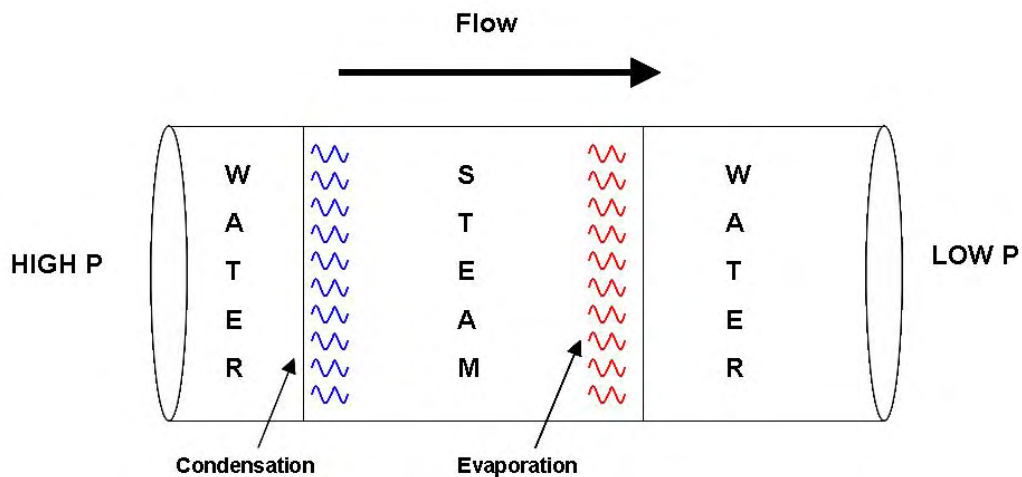


**Figure 3-6. Example of movement of a steam bubble through water in a tube via the phase change mechanism. Steam forms on the down-pressure end of the bubble and condenses at the high-pressure end of the bubble, thus moving the location of the bubble without moving the actual mass in the tube.**

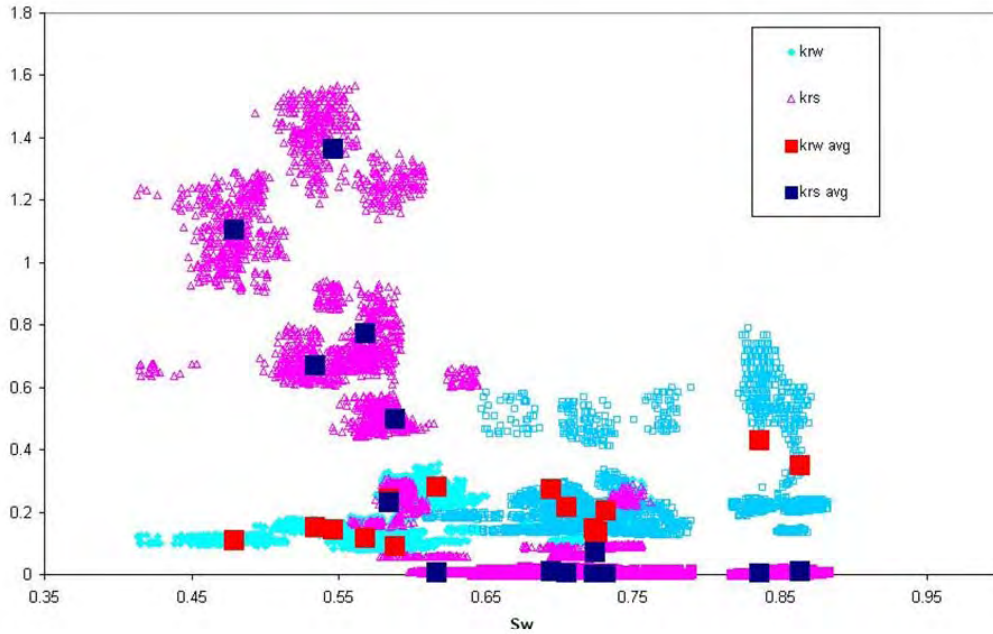


**Figure 3-7. Full and averaged steam-water relative permeability values for the smooth-walled fracture.**

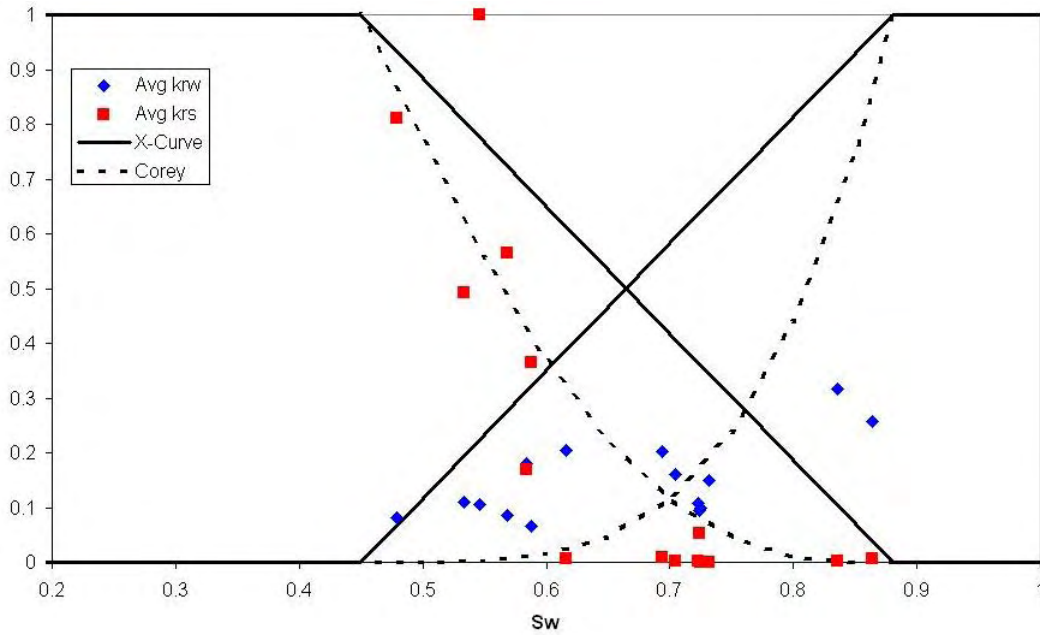


**Figure 3-8. Averaged smooth-walled steam-water relative permeability data normalized and compared with established relative permeability models.**

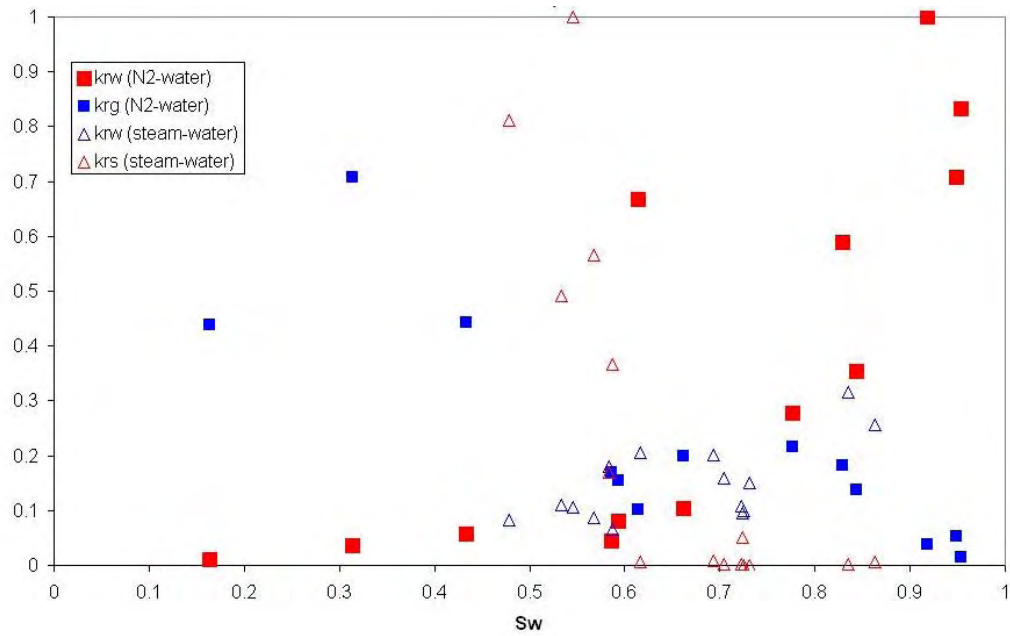


**Figure 3-9. Comparison of normalized steam-water and N<sub>2</sub>-water relative permeability measurements with the smooth-walled fracture.**

### 3.3.2. Rough-Walled Relative Permeability Results

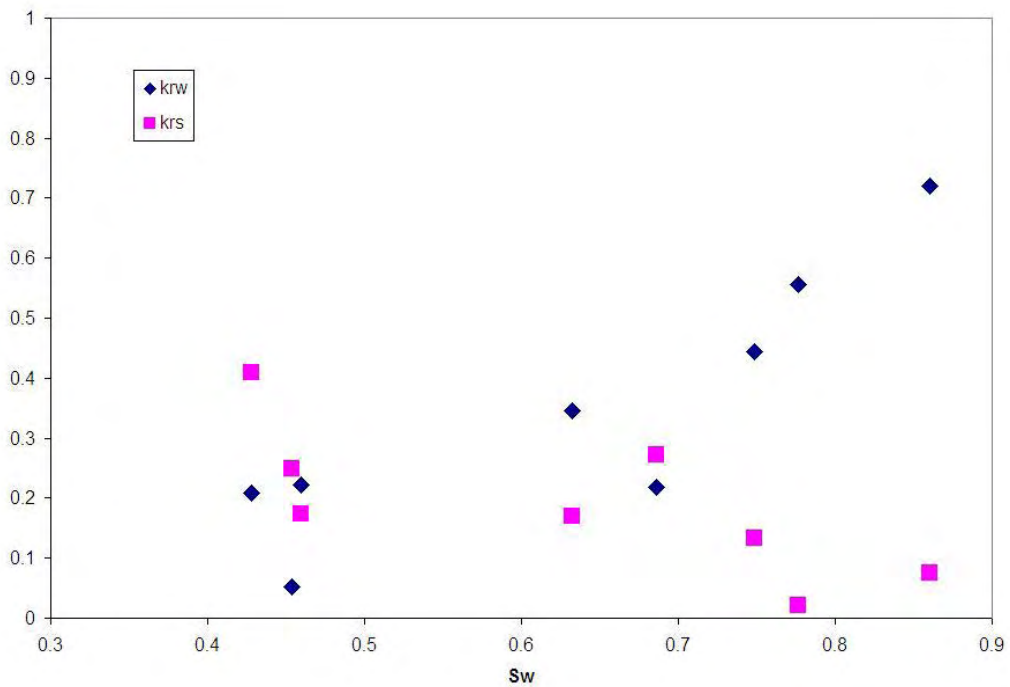


**Figure 3-10. Average steam-water relative permeability values measured on the rough-walled fracture.**

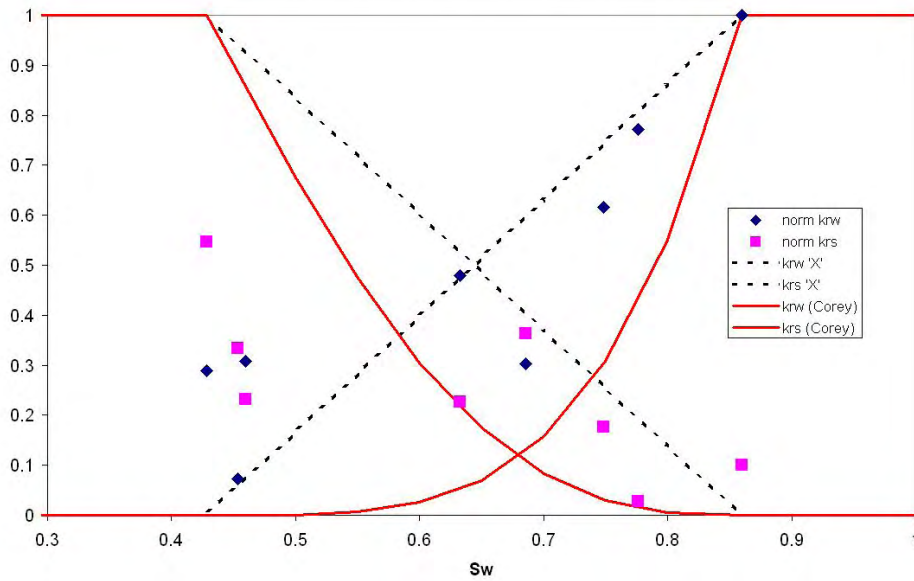


**Figure 3-11. Averaged rough-walled steam-water relative permeability data normalized and compared with established relative permeability models.**

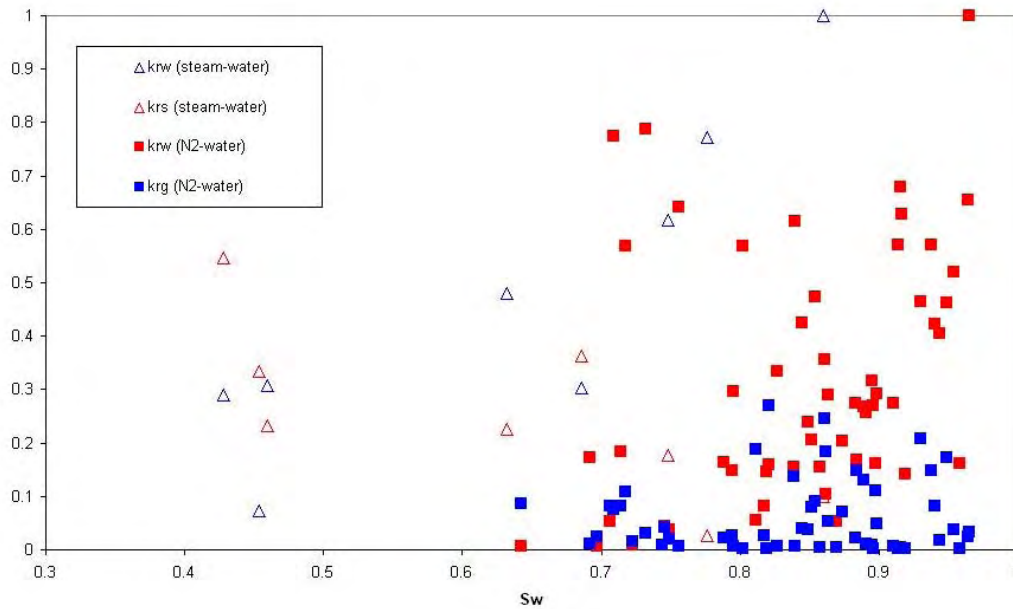


**Figure 3-12. Comparison of normalized steam-water and  $N_2$ -water relative permeability measurements with the rough-walled fracture.**

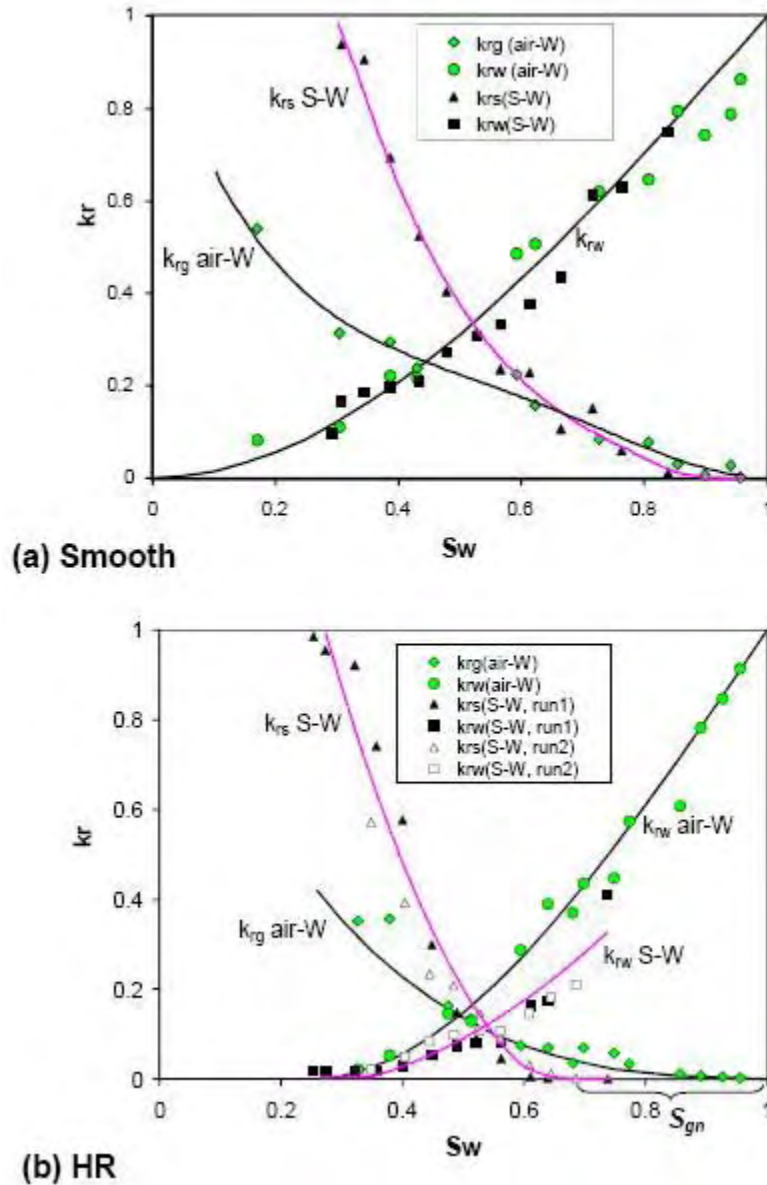


**Figure 3-13. Air-water and steam-water horizontal-fracture relative permeabilities measured on: a) The smooth walled fracture b) The homogeneously rough-walled fracture. Data from Chen, (2005).**

### 3.3.3. Flow Observations

The smooth-walled and rough-walled fractures exhibited significantly different flow characteristics. For the smooth-walled fracture at the initial high-pressure state intended to minimize steam formation, it was impossible to completely eliminate all of the steam in the fracture without raising the pressure beyond the tolerance of the equipment. Very little steam formed in the heating coil, but small steam bubbles would nucleate within the fracture itself (Figure 3-14). This was not an undesirable effect given that in a fracture at steam-saturated conditions, steam and water are changing phase all the time. These

locally nucleated steam bubbles would either stay where they formed or slowly migrate upward and in the direction of flow if they grew large enough. They would leave behind a two-phase tail that appeared to be a film of steam on one fracture surface and water on the other side (Figure 3-15).

As the fracture pressure was lowered, these bubbles continued to form, but steam also formed in the heating coil. The steam formed in the heating coil formed a thin channel along the top edge of the fracture. The nucleated steam bubbles in the fracture continued to form and migrate towards the top of the fracture with increasing frequency. As the fracture pressure was further reduced the steam channel along the top edge increased in thickness and boiling proceeded at a much higher rate within the fracture, producing a very dynamic repeating state with large steam structures rapidly forming and migrating upward to meet the upper channel, only to form again (Figure 3-16).



**Figure 3-14. Static locally nucleated steam bubbles at very low steam-water flow ratios in the smooth-walled fracture. Steam is the dark phase.**



**Figure 3-15. Locally nucleated steam pockets (dark phase) migrating upward and in the direction of flow in the smooth-walled fracture, leaving behind two-phase trails (light gray).**

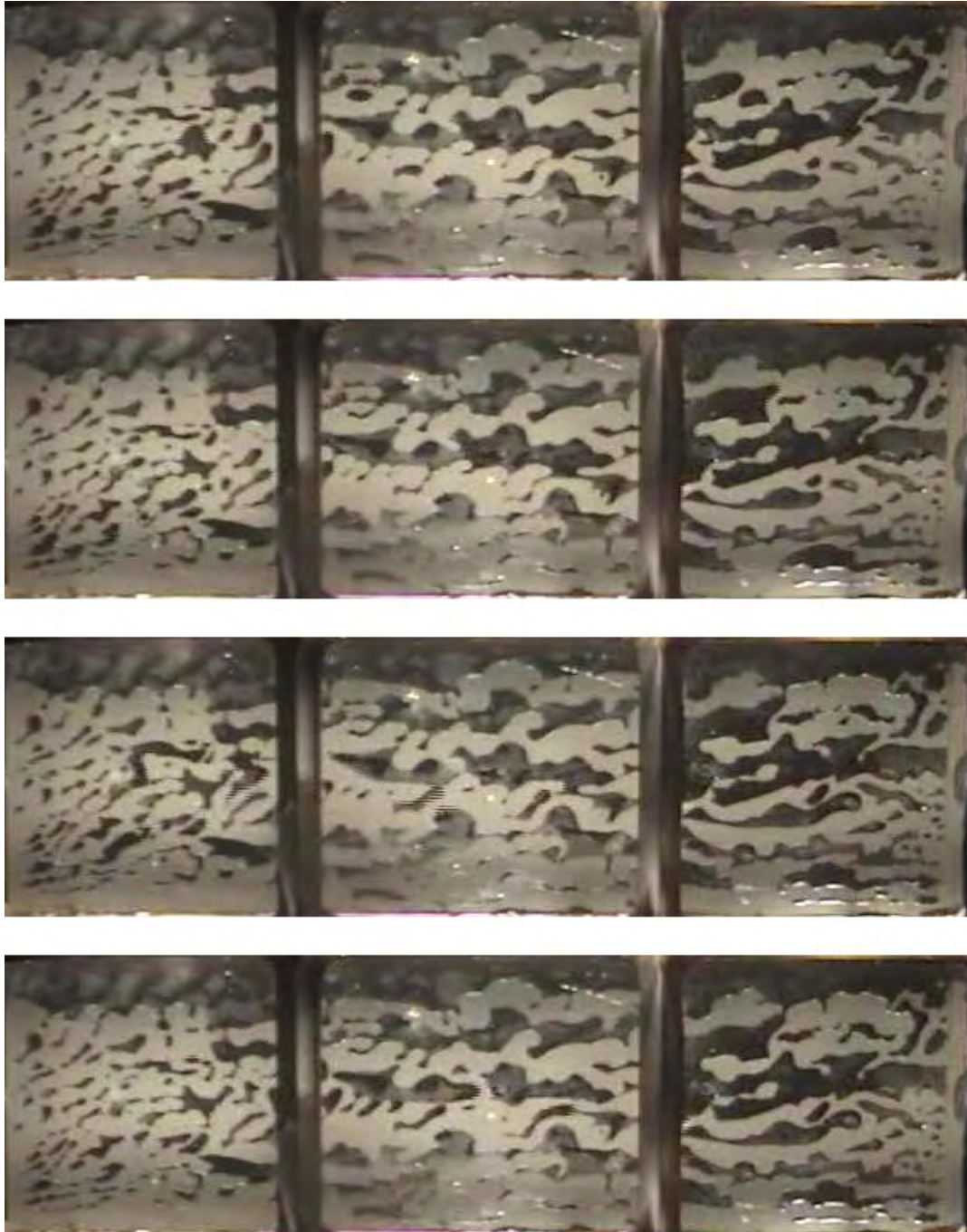


**Figure 3-16. Example of development and movement of steam structures in the smooth-walled fracture with high steam-water ratios. Each frame is separated by 0.4 seconds.**

The rough-walled fracture displayed similar behavior in terms of steam forming a channel along the top wall of the fracture, but the nucleated steam bubbles within the fracture were not nearly as mobile as in the smooth-walled fracture. The steam tended to

stay in place where it was formed (Figure 3-17). Eventually when pressure was dropped enough for steam to really dominate flow through the fracture, the steam formed a series of relatively stable channels, with a greater concentration of steam at the top of the fracture than at the bottom. As a whole, the flow structures in the rough-walled fracture were significantly more stable (Figure 3-18).



**Figure 3-17. Example of steam-water flow structures in the rough-walled fracture with low steam-water flow ratios.**



**Figure 3-18. Example of steam-water flow structures in the rough-walled fracture with high steam-water flow ratios.**

### 3.4. Discussion

#### 3.4.1. Smooth-Walled Fracture

Normalizing the steam-water and N<sub>2</sub>-water relative permeabilities for the smooth-walled fracture and comparing them on the same axes (Figure 3-9), a few trends were visible. First, the  $S_{rw}$  was lower and the  $S_{gi}$  higher for the steam-water experiments. In other words, the range of mobile saturation for the steam was much lower than for the N<sub>2</sub>. Also, the steam relative permeability curve was much steeper than the N<sub>2</sub> curve at low  $S_w$ . The water relative permeability curves were very similar in shape up to the steam  $S_{gi}$ . However, the air-water relative permeability was much steeper at higher  $S_w$ .

Comparing the smooth-walled relative permeabilities with X-curves and Corey-curves (Figure 3-8), the steam curve follows the Corey curve very closely. The water curve does not, but instead it increases somewhat linearly, but not as steeply as the X-curve.

Comparing the smooth-walled relative permeabilities with those measured by Chen on the exact same apparatus oriented horizontally (Figure 3-13a), the steam curve is similar in shape, but the water curve was much steeper for the horizontal fracture.

Orienting the smooth-walled fracture vertically was expected to produce layered, laminar flow, with steam flowing over the water. As stated previously, one of the goals of this study was to see if X-curve relative permeabilities were applicable even at the most likely conditions. They were not.

#### 3.4.2. Rough-Walled Fracture

Normalizing the steam-water and N<sub>2</sub>-water relative permeabilities for the rough-walled fracture and comparing them on the same axes (Figure 3-12), there is not much to see due to the noisy nature of the N<sub>2</sub>-water data, but a few characteristics are still visible. Contrary to the phenomenon observed in the smooth-walled fracture, the mobile saturation range of the steam-water system was much greater than that of the N<sub>2</sub>-water system. However, the steam-water mobile saturation range is almost identical for smooth-walled and rough-walled fractures ( $S_w$  between ~0.45 and ~0.85), so the main difference is between the N<sub>2</sub>-water systems for smooth and rough-walled fractures.

Comparing the rough-walled relative permeabilities with those measured by Chen on the exact same apparatus oriented horizontally (Figure 3-13b), both the shapes and magnitudes are significantly different with the vertical fracture. The magnitudes especially are drastically different for the rough-walled fracture, with maximum measured relative permeability being around 0.3. To verify these small magnitudes, the procedure was repeated, but only to calculate endpoint relative permeability values. The endpoint  $k_{rs}$  was measured as 0.42 and the endpoint  $k_{rw}$  was measured at 0.71. The measured data were fit to these endpoints which were considered more reliable. The endpoint relative permeabilities are roughly twice the original endpoint values, but still significantly lower than 1. These results are shown in Figure 3-10.

Understanding that the magnitude of the relative permeability values for the rough-walled fracture are uncertain, the relative permeability behavior can still be read from the shapes of the curves.

Even assuming the relative permeability values were underestimated due to the  $kA$  bias, there is a great deal of phase interference. The source of this interference is uncertain. It could be that the roughness of the glass provided many more sites for nucleation of small immobile steam bubbles than were provided by the smooth-walled fracture. All of those tiny interfaces could have a very significant impact on overall phase interference. However, there is nothing to suggest that the same in-situ nucleation did not also occur in the fracture oriented horizontally, and yet those results show significantly less phase interference.

The shapes of the measured relative permeability curves were also different from those measured by Chen. The steam curve was not nearly as steep for the vertical fracture, and it did not get as high compared to the water curve.

## Chapter 4

### 4. Conclusions and Future Work

The goal of this study was to build upon the work of Allan Chen and using the same equipment, explore the relative permeability characteristics of horizontal flow in vertical fractures. The X-curve relative permeability curves had been effectively disproved for horizontal fractures, and they have now been shown to be invalid in even the most conducive conditions of laminar flow in a vertical smooth-walled fracture. Even in such conditions, there was significant phase interference both at the main interface between the water and gas channels and around the residual pockets of water and gas left behind in the opposite phase.

As anticipated, the steam relative permeabilities were measured to be generally higher than the comparable gas permeabilities. This can be attributed to the phase transformation effects discussed in Chapter 3. The mobile saturation range for the steam-water system was more or less unchanged by fracture roughness. For the air-water system, increased surface roughness increased  $S_{rw}$  dramatically.

Immobile saturation as it applies to relative permeabilities is a difficult concept in systems with high dissolution and solution rates like  $\text{CO}_2$ -water or systems with significant phase-change effects, like steam-water. Given the right conditions, the residual saturation of a phase can be removed from the system either through a phase change (boiling of residual water) or by solution/dissolution (dissolving of residual  $\text{CO}_2$ ). However, we consider any phase immobile once it cannot move without dissolving or changing phase.

Although most of the data gathered in this study had too much noise to be the basis for a precise model, the data did show some clear relative permeability trends for both steam-water and gas-water flows in smooth and rough-walled fractures.

The experimental apparatus used in this study is very robust in its capabilities, but it leaves some things to be desired. First, it would be nice to simulate flow rates that are on the same scale as those observed in geothermal reservoirs. In this study we were simulating superficial velocities on the order of tens of centimeters per second at most, whereas in geothermal reservoirs, inferred superficial velocities can be orders of magnitude larger. Certainly at such velocities, inertial effects and turbulence have a much greater influence on fluid flow.

It would also be interesting to experiment with a larger fracture or a system of fractures either real or synthetic to determine the relative permeability behavior of fracture

networks and determine if/how relative permeability behavior scales with fracture and network size.

A third avenue worthy of exploration would be to experiment using the current apparatus oriented in different directions, and with flow in different directions: i.e. vertical flow in a vertical fracture, or inclined flow.

## Nomenclature

$A$	= Cross-sectional area of the fracture
$f_w$	= Fractional flow of water
$f_s$	= Fractional flow of steam
$h$	= Fracture Aperture
$k$	= Absolute permeability
$k_{rw}$	= Water relative permeability
$k_{rg}$	= Gas relative permeability
$k_w$	= Water permeability
$k_g$	= Gas permeability
$L$	= Length
$m_{in}$	= Mass input rate
$p_i$	= Inlet pressure
$p_o$	= Outlet pressure
$\Delta p$	= Pressure drop
$q_w$	= Water volumetric flow rate
$q_g$	= Gas volumetric flow rate
$q_s$	= Steam volumetric flow rate
$S_w$	= Wetting phase saturation
$S_{rl}$	= Residual liquid saturation
$S_{rg}$	= Residual gas saturation
$S^*$	= Mobile saturation
$\mu_s$	= Steam viscosity
$\mu_w$	= Water viscosity
$\mu_g$	= Gas viscosity
$\rho_w$	= Water density
$\rho_s$	= Steam density



## References

- Brooks, R.H. and Corey, A.T.: "Properties of Porous Media Affecting Fluid Flow" *J. Irrigation and Drainage Division.*, Proc. ASCE, IR2 (1966), Vol. 92, pp. 61-88.
- Chen, A.: "Liquid-Gas Relative Permeabilities in Fractures: Effects of Flow Structures, Phase Transformation and Surface Roughness". PhD Thesis, Stanford University, Stanford, CA (2005).
- Corey, A.T. "The Interrelation Between Gas and Oil Relative Permeabilities" *Producers Monthly* (1954) Vol. 19, pp. 38-41
- Diomampo, G.P.: "Relative Permeability through Fractures". MS Thesis. Stanford University, Stanford, California (2001).
- Fourar, M., Bories, S., Lenormand, R., Persoff, P.: "Two-phase Flow in Smooth and Rough Fractures: Measurement and Correlation by Porous-Medium and Pipe-flow Models" *Water Resources Research* Vol. 29, No. 11, November 1993, pp. 3699-3708.
- Fourar, M., Lenormand, R.: "A Viscous Coupling Model for Relative Permeabilities in Fractures" SPE 49006, paper presented at the SPE Annual Technical Conference and Exhibition, New Orleans, LA, USA. 1998.
- Persoff, P. and Pruess, K.: "Two-phase Flow Visualization and Relative Permeability Measurement in Natural Rough-walled Rock Fractures", *Water Resources Research* Vol. 31, No. 5, May 1995, pp. 1175-1186.



# Appendix A

## A. Matlab Code for Image Capture

```
%%% Image Capture program for short timestep    Chih-Ying Chen  2003/2/25
%%% Modified by Nick Speyer October 2006
clear all
disp('This program will capture images from the AVI file you specified')
disp('The default avi frame rate is 30frames/sec.')

rate=30 % avi default rate; #frame/sec
oriVideo=input('Input the video filename you wanna capture:', 's')
%filehead=input('Input head of output filenames:', 's');
iniSec=input('Input the initial time when you wanna start capturing the
image: (sec., =0 first frame)')
flag=0;
while flag==0;
    jump=input('Input the frame number you want to pass by:')
    iniFrame=iniSec*rate+jump;
    mov=aviread(oriVideo, iniFrame);
    img=frame2im(mov);
    imshow(img);
    flag=input('Is this image close enough? (1=yes, 0=no)')
end
count=input('Input the exact time representing the first image (without
:):')
count2=count*10+1;
period=input('Input the period of the video you want to extract:
(sec)');
freq=input('Input the frequency of the image extraction,
f=images/extraction >3 (f has to be a factor of 30, ex. f=30 =>
30img/ext =>1 img/sec)');
aftersec=rate/freq;
if rem(rate, freq) ~= 0
    error ('Invalid frequency!')
end
totalF=iniFrame+rate*period;
subDir=int2str(count)
mkdir(subDir);
%Check error
if totalF/freq > 5500
    error('The total number of captured image files is exceed 5500. We
suggest you to use a larger frequency of short period (<30min).!!!')
end
output=fullfile(pwd, subDir, 'filenameArray.txt');
fid=fopen(output, 'w');

for i=iniFrame:freq:totalF
    mov=aviread(oriVideo, i);
    img=frame2im(mov);
```

```

remlst=rem(count2,1000);
if remlst > 599
    count2=count2+1001-remlst;
    rem2nd=rem(count2,100000);
    if rem2nd > 59599
        count2=count2+100001-rem2nd;
    end
end
time=int2str(count2);
fileName=strcat(time, '.jpg')
f=fullfile(pwd,subDir,fileName);
imwrite(img,f,'Quality',100);
fprintf(fid,'%s \n',fileName);
if rem(count2,10)<aftersec
    count2=count2+1;
else
    count2=count2-rem(count2,10)+11;
end
end
disp('===== Job finished =====')
freq
period
iniSec
fclose(fid);

```

## Appendix B.

### B. Matlab Code for $S_w$ Calculation (Rough-Walled)

```
%%% This is the new version for the saturation calculation.      Written
by Allan Chen 03/25/2004
%%% Modified by Nick Speyer November 2006
%% Program name: DSWC; Discretized Saturation Calculation.
% This algorithm of this program is "not" based on LDA, but on
discretized
% thresholds in each sub images. This program first discretizes the
whole
% image to several sub images based on the background intensity
variation,
% and then converts each subimage to binary image based on the
corresponding threshold
% obtained by trial-n-error. Then it reconstructs the whole images.

clear all;
close all;

%%%%%%%%%%%%%%%%%%%%%%%%%%%%%%%%%%%%%%%%%%%%%%%%%%%%%%%%%%%%%%%%%%%%%%%% parameter input
%%% couoff info. (you have to input the correct info.
ref:220,50,650,100)
Ymax = 275
Ymin = 130
Xmax = 461
Xmin = 280
map=[0 0 0;1 1 1];
%stripcolmin=100
%stripcolmax=450
%% Coordinates
y1=30;y11=60;y2=90;y3=115;
x1=30;x2=60;x3=90;x4=120;x5=150;
%% Binary threshold
%% ref:th11=0.295;th12=0.3;th13=0.235;th21=0.36;th22=0.42;th23=0.28;
%%      th31=0.42;th32=0.385;th33=0.295;th34=0.55;th35=0.35;
%%      th41=0.38;th42=0.49;th43=0.42;sth=0.17
%sth=0.17;

th11=0.25;th12=0.26;th13=0.19;
th21=0.23;th22=0.23;th23=0.18;
thA1=0.22;thA2=0.24;
th31=0.27;th32=0.23;th33=0.23;th34=0.25;th35=0.2;
th41=0.22;th42=0.22;th43=0.21;

%%%%%%%%%%%%%%%%%%%%%%%%%%%%%%%%%%%%%%%%%%%%%%%%%%%%%%%%%%%%%%%%%%%%%%%%

% This part will ask user for the image to be processed.
disp(' Exclude Strip!, Cut some edge off');
filenameArray % input filenames data file
```

```

disp('total number of files')
totalfiles=length(fileArray)
disp('')
counter=input('Input the initial counter of this job: (new job
counter=1)');
File = string(char(fileArray(counter)));

Image = imread(File);
figure,image(Image);
grid on

cutImg = Image(Ymin:Ymax, Xmin:Xmax, :);
cutfilename=strcat('cf',File);
imwrite(cutImg, cutfilename);
%%%%%
I=rgb2gray(cutImg);
[rImg,cImg]=size(I);
%%% Metal strip calculation
%cutImgS=I(1:rImg,stripcolmin:stripcolmax);
%figure,imshow(cutImgS);
%Kstrip2 = im2bw(cutImgS,sth);
%Kstrip = IMFILL(Kstrip2,8,'holes');
%figure, imshow(Kstrip)
colormap(map);
%stripix=sum(sum(~Kstrip))

figure,image(cutImg);
text(3,5, File)
np=1;
subDSWC16 %% calc Sw
Answer(1,:)={File Sw};

aa=randperm(50);
bb=aa(10);
cc=int2str(bb);
output=strcat('output',cc, '.txt')
fid=fopen(output,'w');
fprintf(fid,'%s %8.4f \n',File, Sw);

another =input('another? 1-yes, 2-no:');
while (another ==1)
    counter=counter+1;
    close all;
    File = string(char(fileArray(counter)))
    Image = imread(File);
    cutImg = Image(Ymin:Ymax, Xmin:Xmax, :);
    I=rgb2gray(cutImg);
    cutfilename=strcat('cf',File);
    imwrite(cutImg, cutfilename);
    np=counter;
    subDSWC16;
    Answer(counter,:)={File Sw};
    fprintf(fid,'%s %8.5f \n',File, Sw);
    if counter>=totalfiles % check stop criterion
        another=2;
        disp('Finish all of the discrimination!')
    end
end
end
Answer

```

```
disp('    === Please save the answer right now in case you erase it!!')
counter
totalfiles
disp('===== output Sw file name: ')
output

fclose(fid);
```

# Appendix C

## C. Matlab Codes for $S_w$ Calculation (Smooth-Walled)

### Main Code: LDAv2full.m

```
% This is the testing modifying version done by Allan 02/19/2002
% Modified by Nick Speyer in March 2007
% This program calculate the saturation of two phase area.
% It is done by linear discriminant method.
% It will input the filenames datafile (fileArray) which was
% created by you, and it will do the batch run.
% Original version was credited to G. Diomampo

clear all;
close all;

% This part will ask user for the image to be processed.
disp('This program will cut off the first window and end range. No Strip
calc here');

filenametest % input filenames data file

disp('total number of files')
totalfiles=length(fileArray)
disp('')
counter=input('Input the initial counter of this job: (new job
counter=1)');
File = string(char(fileArray(counter)));
figure;
Image = imread(File);
stripix=11674 %(2a)
disp('ref 215 50 665 60');

image(Image);
grid on
Sentinel = 0;
iter = 1;
FileNo = 1;

%% couoff info. (you have to input the correct info.)
Ymax = 263
Ymin = 79
Xmax = 487
Xmin = 278
cutImg = Image(Ymin:Ymax, Xmin:Xmax, :);
figure;
image(cutImg);
text(3,5, File)
```

```

%%%%%%%%

[rImg,cImg]=size(cutImg);
cutpix=rImg*cImg  %(A)
sample = GenerateSample(cutImg);

%generation of phase data set
NtrnL=input('No. of liquid sample data: ');
liq = GetTrainingData(cutImg);
for i=1:(NtrnL-1)
    liqNew = GetTrainingData(cutImg);
    trnl=[liq;liqNew];
end

trl=CheckVariance(trnl);

Ntrng=input('No. of gas sample data: ');
gas = GetTrainingData(cutImg);
for i=1:(Ntrng-1)
    gasNew = GetTrainingData(cutImg);
    trng=[gas;gasNew];
end

trg=CheckVariance(trng);

trn =[trl;trg];

%generation of grouping
[RTr1,CTr1] = size(trnl);
[RTr2,CTr2] = size(trng);
%[RTr3,CTr3] = size(trnstp);
grp1 = ones(RTr1,1);
grp2 = ones(RTr2,1).*2;
%grp3 = ones(RTr3,1).*3;

grp=[grp1;grp2];

DoClassification
cutfilename=strcat('cf',File);
imwrite(cutImg, cutfilename);

Answer(1,:){File Sw};

aa=randperm(50);
bb=aa(10);
cc=int2str(bb);
output=strcat('output',cc, '.txt')
fid=fopen(output, 'w');
fprintf(fid, '%s %8.4f \n',File, Sw);

another =input('another? 1=yes, 2=no: ');
while (another ==1)
    counter=counter+1;
    close all;
    File = string(char(fileArray(counter)))
    %figure;

```

```

Image = imread(File);
%image(Image);
cutImg = Image(Ymin:Ymax, Xmin:Xmax, :);
%figure;
%image(cutImg);
cutfilename=strcat('cf',File);
imwrite(cutImg, cutfilename);
[rImg,cImg]=size(cutImg);
sample = GenerateSample(cutImg);
DoClassification
Answer(counter, :)= {File Sw};
fprintf(fid, '%s %8.5f \n', File, Sw);
% another = input('another? 1=yes,2=no:');
if counter>=totalfiles % check stop criterion
    another=2;
    disp('Finish all of the discrimination!')
end
end
Answer
disp('==== Please save the answer right now in case you erase it!!')
counter
totalfiles
disp('===== output Sw file name: ')
output

fclose(fid);

```

### SubRoutine: CheckVariance.m

```

function trl = CheckVariance(trnl)

varl=var(trnl);
[row,col]=size(trnl);
err=0.001*rand(row,1);

if (varl(1,1)==0)
    trnl1=trnl(:,1)+err;
else
    trnl1=trnl(:,1);
end

if (varl(1,2)==0)
    trnl2=trnl(:,2)+err;
else
    trnl2=trnl(:,2);
end

if (varl(1,3)==0)
    trnl3=trnl(:,3)+err;
else
    trnl3=trnl(:,3);
end

```

```
tr1=[trn11 trn12 trn13];
```

### SubRoutine: DoClassification.m

```
%Written by Allan Chen, modified by Nick Speyer
%function DoClassification(sample, trn, grp, File, rImg,cImg)
stripix=0;
clas =classify(sample,trn,grp);
classImg =reshape(clas,rImg,cImg/3);
figure;
imagesc(classImg);
colormap(gray);
Sweva = sum(clas==1)/(sum(clas==1)+sum(clas==2))
Sgeva=1-Sweva;
Sg=(Sgeva-stripix/cutpix)*cutpix/(cutpix-stripix);
Sw=1-Sg
text(1,1,File, 'Color', 'r');
satString = num2Str(Sw);
satLabel = strcat('Sw=', satString)
xlabel(satLabel);
bwfilename=strcat('bw',File);
classImg2=35*ind2gray(classImg, gray);
imwrite(classImg2, bwfilename);
%[firt,bck]=strtok(File,'b');
%name=strrep(bck,'b\',' ');
```

### SubRoutine: GenerateSample.m

```
% This part will create the group based on the number of rows of tr1 and tr2
```

```
function sample = GenerateSample(cutImg)
```

```
red = double(cutImg(:,:,1));
green = double(cutImg(:,:,2));
blue = double(cutImg(:,:,3));
sample=[red(:),green(:),blue(:)];
```

```
GenerateSample = sample;
```

### SubRoutine: GetTrainingData.m

```
function Trn = GetTrainingData(image)
```

```
% This function creates a matrix of training data using the polygon
% specified by the user
```

```
red = double(image(:,:,1));
green = double(image(:,:,2));
blue = double(image(:,:,3));
```

```
mask1=roipoly;
fprintf('Using this image, creat a polygon to represent the phase\n');
trn1r = red(mask1);
```

```
trnlg = green(mask1);
trnlb = blue(mask1);
Trn=[trnlr trnlg trnlb];
```

## Appendix D

### D. FFRD Matlab Code

```
%2/22/07 Nick Speyer%
%Load FFRD data and plot histogram%

clear all
close all
clc
vector = load('ffrd_1.8_after.txt');
vector(1,1)=vector(2,1);
%Moving average calculation to smooth out noisy data, use sparingly!
% for i=4:(max(size(vector))-2)
%     AvgVec(1,i-2)=1/5*(vector((i-2),1)+vector((i-
1),1)+vector(i,1)+vector((i+1),1)+vector((i+2),1));
% end
nbins=10
hist(vector,nbins);

cutoff=input('Enter Cutoff Value and Press Enter: ');

steam=1;
water=1;
for counter=1:max(size(vector));
    if(vector(counter,1)<cutoff)
        steam=steam+1;
    else
        water=water+1;
    end
    counter=counter+1;
end
fw=water/(water+steam)
fs=steam/(water+steam)
```